Comput. Methods Appl. Mech. Engrg. 417 (2023) 116471

Contents lists available at ScienceDirect

Comput. Methods Appl. Mech. Engrg.

journal homepage: www.elsevier.com/locate/cma

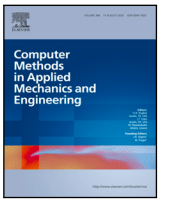

Adjoint-based determination of weaknesses in structures

Facundo N. Airaudo [a], Rainald Löhner [a,*], Roland Wüchner [b], Harbir Antil [c]

[a] Center for Computational Fluid Dynamics and Department of Physics and Astronomy, George Mason University, Fairfax, VA 22030, USA
[b] Institut für Statik und Dynamik — Institute of Structural Analysis, Beethovenstrasse 51, 38106 Braunschweig, Germany
[c] Center for Mathematics and Artificial Intelligence (CMAI) and Department of Mathematical Sciences, George Mason University, Fairfax, VA 22030, USA

ARTICLE INFO

Keywords:
Weakness detection
Digital twin
Adjoint methods
Finite elements
Sensor embedding
Lifetime monitoring of structures

ABSTRACT

An adjoint-based procedure to determine weaknesses, or, more generally the material properties of structures is developed and tested. Given a series of force and displacement/strain measurements, the material properties are obtained by minimizing the adequately weighted differences between the measured and computed values. The approach is directly based on the finite element model of the structure of interest, which can be arbitrarily complex and be composed of any kind of element formulation. This is especially advantageous in complicated real-world applications. As a consequence, the procedure can provide highly resolved parameter distributions within the structure and allows for the localization of e.g. damage regions or other zones with deviations from the planned configuration. Several examples with truss, plain strain and volume elements show the viability, accuracy and efficiency of the proposed methodology using both displacement and strain measurements. An important finding was that in order to obtain reliable, convergent results the gradient of the cost function has to be smoothed appropriately.

1. Introduction

The problem of trying to determine the material properties of a domain from loads and measurements is common to many fields. To mention just a few: mining (e.g. prospecting for oil and gas), medicine (e.g. trying to infer tissue properties), engineering (e.g. trying to determine the existence and location of fissures, aging of structures).

A very pressing issue at present is the aging of concrete structures in the developed world. Many bridges (and large buildings) were built with reinforced concrete after the destruction of the second world war and the highway system that emerged thereafter. These bridges are now 60–70 years old, about the lifespan of concrete. Therefore, it is imperative to know their structural integrity, which implies determining material properties from external loads and displacements. Damage localization is especially challenging in the case of reinforced concrete structures due to the inhomogeneous material layout and (mostly) very voluminous, massive structures. Another prominent example with urgent need for damage identification are the structures in wind generators [1]. These massive devices are continuously subjected to large, time-dependent forces which will surely lead to material exhaustion and aging in 20–50 years. This motivates the development of new damage detection techniques suitable for these applications. As is usual in the empirical sciences, both experimental (as is, in vivo) and analytical techniques are being pursued vigorously at present.

On the experimental side, vibration analysis, coda wave interferometry [2–4], external and internal laser interferometry, and even in-situ X-ray techniques are being considered.

* Corresponding author.
E-mail addresses: fairaudo@gmu.edu (F.N. Airaudo), rlohner@gmu.edu (R. Löhner), r.wuechner@tu-braunschweig.de (R. Wüchner), hantil@gmu.edu (H. Antil).

https://doi.org/10.1016/j.cma.2023.116471
Received 27 March 2023; Received in revised form 19 September 2023; Accepted 19 September 2023
Available online xxxx

On the analytical side, many techniques have been developed over the last decades [5–16]. Some of these were developed to identify weaknesses in structures, others (e.g. [6]) to correct or update finite element models. The damage/weakness detection from measurements falls into the more general class of inverse problems where material properties are sought based on a desired cost functional [14,17–19]. It is known that these inverse problems are ill-defined and require regularization techniques.

The analytical methods depend on the measurement device at hand, and one can classify broadly according to them. The first class of analytical methods is based on changes observed in (steady) displacements or strains [10,12,15,16,20]. The second class considers velocities or accelerations in the time domain [8,9,13]. The third class is based on changes observed in the frequency domain [5–7,11,14].

Some of the methods based on displacements, strains, velocities or accelerations used adjoint formulations [10,12,13,20–23] in order to obtain the gradient of the cost function with the least amount of effort.

The procedures proposed here are also based on measured forces and displacements/strains, use adjoint formulations and smoothing of gradients to quickly localize damaged regions. Unlike previous efforts, they are intended for weakness/damage detection in the context of digital twins, i.e. we assume a set of defined loadings and sensors that accompany the structure (object, product, process) throughout its lifetime in order to monitor its state. The digital twins are assumed to contain finite element discretizations/models of high fidelity, i.e. it is important to show the use of multiple element types in order to ensure the generality of the proposed procedures. In order to ensure convergence, an appropriate infinite dimensional scaling (scalar product) is used to evaluate the gradients. This is also termed as gradient smoothing. Several of the numerical examples clearly indicate that in order to obtain convergence, it is critical to account for this smoothing.

The framework introduced has been applied to multiple challenging examples including bridges, cranes, plates and solids.

2. Determining material properties via optimization

The determination of material properties (or weaknesses) may be formulated as an optimization problem for the strength factor $\alpha(\mathbf{x})$ as follows: Given n force loadings $\mathbf{f}_i, i = 1,n$ and n measurements at m measuring points/locations $\mathbf{x}_j, j = 1,m$ of their respective displacements $\mathbf{u}_{ij}^{md},\ i = 1,n,\ j = 1,m$ or strains $\mathbf{s}_{ij}^{ms},\ i = 1,n,\ j = 1,m$, obtain the spatial distribution of the strength factor α that minimizes the cost function:

$$I(\mathbf{u}_{1,\dots,n},\alpha) = \frac{1}{2}\sum_{i=1}^{n}\sum_{j=1}^{m} w_{ij}^{md}(\mathbf{u}_{ij}^{md} - \mathbf{I}_{ij}^{d}\mathbf{u}_i)^2 + \frac{1}{2}\sum_{i=1}^{n}\sum_{j=1}^{m} w_{ij}^{ms}(\mathbf{s}_{ij}^{ms} - \mathbf{I}_{ij}^{s}\mathbf{s}_i)^2 \tag{2.1}$$

subject to the finite element description (e.g. trusses, beams, plates, shells, solids) of the structure [24,25] under consideration (i.e. the digital twin/system [26,27]):

$$\mathbf{K}\mathbf{u}_i = \mathbf{f}_i\ ,\quad i = 1,n\ , \tag{2.2}$$

where w_{ij}^{md}, w_{ij}^{ms} are displacement and strain weights, $\mathbf{I}^d, \mathbf{I}^s$ interpolation matrices that are used to obtain the displacements and strains from the finite element mesh at the measurement locations, and $\mathbf{K}$ the usual stiffness matrix, which is obtained by assembling all the element matrices:

$$\mathbf{K}_{ij} = \sum_{e=1}^{N_e} \alpha_e \mathbf{K}_{ij}^{e}\ , \tag{2.3}$$

where the strength factor α_e of the elements has already been incorporated. In order to ensure that $\mathbf{K}$ is invertible and non-degenerate $\alpha_e > \epsilon > 0$, where ϵ is a cut-off that is typically set to $\epsilon = O(10^{-2})$. We emphasize that the optimization problem (2.1)–(2.2) does not assume any specific choice of finite element basis functions, but it is widely applicable.

2.1. Optimization via adjoints

The objective function can be extended to the Lagrangian functional

$$L(\mathbf{u}_{1,\dots,n},\alpha,\tilde{\mathbf{u}}_{1,\dots,n}) = I(\mathbf{u}_{1,\dots,n},\alpha) + \sum_{i=1}^{n}\tilde{\mathbf{u}}_i^t(\mathbf{K}\mathbf{u}_i - \mathbf{f}_i)\ , \tag{2.4}$$

where $\tilde{\mathbf{u}}_i$ are the Lagrange multipliers (adjoints). Variation of the Lagrangian with respect to each of the measurements then results in:

$$\frac{dL}{d\tilde{\mathbf{u}}_i} = \mathbf{K}\mathbf{u}_i - \mathbf{f}_i = 0 \tag{2.5a}$$

$$\frac{dL}{d\mathbf{u}_i} = \sum_{j=1}^{m} w_{ij}^{md}\mathbf{I}_{ij}^{d}(\mathbf{u}_{ij}^{md} - \mathbf{I}_{ij}^{d}\mathbf{u}_i) + \sum_{j=1}^{m} w_{ij}^{ms}\mathbf{J}_{ij}^{s}(\mathbf{s}_{ij}^{ms} - \mathbf{I}_{ij}^{s}\mathbf{s}_i) + \mathbf{K}^t\tilde{\mathbf{u}}_i = 0 \tag{2.5b}$$

$$\frac{dL}{d\alpha_e} = \sum_{i=1}^{n}\tilde{\mathbf{u}}_i^t\frac{d\mathbf{K}}{d\alpha_e}\mathbf{u}_i = \sum_{i=1}^{n}\tilde{\mathbf{u}}_i^t\mathbf{K}^e\mathbf{u}_i\ , \tag{2.5c}$$

where $\mathbf{J}_{ij}^{s}$ denotes the relationship between the displacements and strains (i.e. the derivatives of the displacement field on the finite element mesh and the location $\mathbf{x}_j$ (see Section 3 below).

The consequences of this rearrangement are profound:

- The gradient of L, I with respect to α may be obtained by solving n forward and adjoint problems; i.e.
- Unlike finite difference methods, which require at least n forward problems per design variable, the number of forward and adjoint problems to be solved is **independent of the number of variables used for** α (!);
- Once the n forward and adjoint problems have been solved, the cost for the evaluation of the gradient of each design variable α_e only involves the degrees of freedom of the element, i.e. is of complexity $O(1)$;
- For most structural problems $\mathbf{K} = \mathbf{K}^t$, so if a direct solver has been employed for the forward problem, the cost for the evaluation of the adjoint problems is negligible;
- For most structural problems $\mathbf{K} = \mathbf{K}^t$, so if an iterative solver is employed for the forward and adjoint problems, the preconditioner can be re-utilized.

2.2. Optimization steps

An optimization cycle using the adjoint approach is then composed of the following steps:
For each force/measurement pair i:

1. With current α: solve for the displacements $\rightarrow \mathbf{u}_i$
2. With current α, $\mathbf{u}_i$ and $\mathbf{u}_{ij}^{md}, \mathbf{s}_{ij}^{md}$: solve for the adjoints $\rightarrow \tilde{\mathbf{u}}_i$
3. With $\mathbf{u}_i, \tilde{\mathbf{u}}_i$: obtain gradients $\rightarrow I_{,\alpha}^i = L_{,\alpha}^i$
4. Once all the gradients have been obtained:
   - 4.1. Sum up the gradients $\rightarrow I_{,\alpha} = \sum_{i=1}^n I_{,\alpha}^i$
   - 4.2. If necessary: smooth gradients $\rightarrow I_{,\alpha}^{smoo}$
   - 4.3. Update $\alpha_{new} = \alpha_{old} - \gamma I_{,\alpha}^{smoo}$.

Here γ is a small stepsize that can be adjusted so as to obtain optimal convergence (e.g. via a line search).

3. Interpolation of displacements and strains

The location of a displacement or strain gauge may not coincide with any of the nodes of the finite element mesh. Therefore, in general, the displacement $\mathbf{u}_i$ at a measurement location $\mathbf{x}_i^m$ needs to be obtained via the interpolation matrix $\mathbf{I}_i^d$ as follows:

$$\mathbf{u}_i(\mathbf{x}_i^m) = \mathbf{I}_i^d(\mathbf{x}_i^m)\mathbf{u} \quad , \tag{3.1}$$

where $\mathbf{u}$ are the values of the displacement vector at all grid points.

In many cases it is much simpler to install strain gauges instead of displacement gauges. In this case, the strains need to be obtained from the displacement field. This can be written formally as:

$$\mathbf{s} = \mathbf{D}\mathbf{u} \quad , \tag{3.2}$$

where the 'derivative matrix' $\mathbf{D}$ contains the local values of the derivatives of the shape-functions of $\mathbf{u}$. The strain at an arbitrary position $\mathbf{x}_i^m$ is obtained via the interpolation matrix $\mathbf{I}_i^s$ as follows:

$$\mathbf{s}_i(\mathbf{x}_i^m) = \mathbf{I}_i^s(\mathbf{x}_i^m)\mathbf{s} = \mathbf{I}_i^s(\mathbf{x}_i^m)\mathbf{D}\mathbf{u} \quad . \tag{3.3}$$

Note that in many cases the strains will only be defined in the elements, so that the interpolation matrices for displacements and strains may differ.

4. Choice of weights

The cost function is given by Eq. (2.1) repeated here for clarity:

$$I(\mathbf{u}_n, \alpha) = \frac{1}{2}\sum_{i=1}^{n}\sum_{j=1}^{m} w_{ij}^{md}(\mathbf{u}_{ij}^{md} - \mathbf{I}_{ij}^d\mathbf{u}_i)^2 + \frac{1}{2}\sum_{i=1}^{n}\sum_{j=1}^{m} w_{ij}^{ms}(\mathbf{s}_{ij}^{ms} - \mathbf{I}_{ij}^s\mathbf{s}_i)^2 \, . \tag{4.1}$$

One can immediately see that the dimensions of displacements and strains are different. This implies that the weights should be chosen in order that all the dimensions coincide. The simplest way of achieving this is by making the cost function dimensionless. This implies that the displacement weights w_{ij}^{md} should be of dimension [1/(displacement*displacement)] (the strains are already dimensionless). Furthermore, in order to make the procedures more generally applicable they should not depend on a particular choice of measurement units (metric, imperial, etc.). This implies that the weights for the displacements and strains should be of the order of the characteristic or measured magnitude. Several options are possible:

Local weighting

In this case

$$w_{ij}^{md} = \frac{1}{(\mathbf{u}_{ij}^{md})^2} \quad ; \quad w_{ij}^{ms} = \frac{1}{(\mathbf{s}_{ij}^{ms})^2} \quad ; \tag{4.2}$$

this works well, but may lead to an 'over-emphasis' of small displacements/strains that are in regions of marginal interest.

Average weighting

In this case one first obtains the average of the absolute value of the displacements/strains for a load case and uses them for the weights, i.e.:

$$u_{av} = \frac{\sum_{j=1}^{m} |\mathbf{u}_{ij}^{md}|}{m} \quad ; \quad w_{ij}^{md} = \frac{1}{u_{av}^2} \quad ; s_{av} = \frac{\sum_{j=1}^{m} |\mathbf{s}_{ij}^{ms}|}{m} \quad ; \quad w_{ij}^{ms} = \frac{1}{s_{av}^2} \quad ; \tag{4.3}$$

this works well, but may lead to an 'under-emphasis' of small displacements/strains that may occur in important regions;

Max weighting

In this case one first obtains the maximum of the absolute value of the displacements/strains for a load case and uses them for the weights, i.e.:

$$\begin{aligned} u_{max} &= max(|\mathbf{u}_{ij}^{md}|, j = 1, m) \quad ; \quad w_{ij}^{md} = \frac{1}{u_{max}^2} \quad ; \\ s_{max} &= max(|\mathbf{s}_{ij}^{ms}|, j = 1, m) \quad ; \quad w_{ij}^{ms} = \frac{1}{s_{max}^2} \quad ; \end{aligned} \tag{4.4}$$

this also works well for many cases, but may lead to an 'under-emphasis' of smaller displacements/strains that can occur in important regions;

Local/max weighting

In this case

$$w_{ij}^{md} = \frac{1}{max(\epsilon u_{max}, |\mathbf{u}_{ij}^{md}|)^2} \quad ; \quad w_{ij}^{ms} = \frac{1}{max(\epsilon s_{max}, |\mathbf{s}_{ij}^{ms}|)^2} \quad ; \tag{4.5}$$

$$w_{ij}^{md} = \frac{1}{max(\epsilon u_{max}, |\mathbf{u}_{ij}^{md}|)^2} \quad ; \quad w_{ij}^{ms} = \frac{1}{max(\epsilon s_{max}, |\mathbf{s}_{ij}^{ms}|)^2} \quad ; \tag{4.6}$$

with $\epsilon = O(0.01 - 0.10)$; this seemed to work best of all, as it combines local weighting with a max-bound minimum for local values.

5. Smoothing of gradients

The gradients of the cost function with respect to α allow for oscillatory solutions. One must therefore smooth or 'regularize' the spatial distribution. This happens naturally when using few degrees of freedom, i.e. when α is defined via other spatial shape functions (e.g. larger spatial regions of piecewise constant α [10]). As the (possibly oscillatory) gradients obtained in the (many) finite elements are averaged over spatial regions, an intrinsic smoothing occurs. This is not the case if α and the gradient are defined and evaluated in each element separately, allowing for the largest degrees of freedom in a mesh and hence the most accurate representation.

Three different types of smoothing or 'regularization' were considered. All of them start by performing a volume averaging from elements to points:

$$\alpha_p = \frac{\sum_e \alpha_e V_e}{\sum_e V_e} \quad , \tag{5.1}$$

where α_p, α_e, V_e denote the value of α at point p, as well as the values of α in element e and the volume of element e, and the sum extends over all the elements surrounding point p.

5.1. Simple point/element/point averaging

In this case, the values of α are cycled between elements and points. When going from point values to element values, a simple average is taken:

$$\alpha_e = \frac{1}{n_e} \sum_i \alpha_i \quad , \tag{5.2}$$

where n_e denotes the number of nodes (degrees of freedom) of an element and the sum extends over all the nodes of the element. After obtaining the new element values via Eq. (5.2) the point averages are again evaluated via Eq. (5.1). This form of averaging is very crude, but works surprisingly well.

5.2. Laplacian smoothing

In this case, the initial values α_0 obtained for α are smoothed via:

$$\left[1 - \lambda \nabla^2\right] \alpha = \alpha_0 \quad , \quad \alpha_{,n}\big|_\Gamma = 0 \tag{5.3}$$

(see Appendix for further details). Note the appearance of the Laplacian operator multiplied by a small (hence the name) 'smoothing factor' λ, which is a free parameter that may be problem and mesh dependent (its dimensional value is length squared). Discretization via finite elements yields:

$$\left[\mathbf{M}_c + \lambda \mathbf{K}_d\right] \boldsymbol{\alpha} = \mathbf{M}_{p1p0} \boldsymbol{\alpha}_0 \quad , \tag{5.4}$$

where $\mathbf{M}_c, \mathbf{K}_d, \mathbf{M}_{p1p0}$ denote the consistent mass matrix, the stiffness or 'diffusion' matrix obtained for the Laplacian operator and the projection matrix from element values ($\boldsymbol{\alpha}_0$) to point values ($\boldsymbol{\alpha}$).

5.3. Pseudo-Laplacian smoothing

One can avoid the dimensional dependency of λ by smoothing via:

$$\left[1 - \lambda \nabla h^2 \nabla\right] \alpha = \alpha_0 \quad , \tag{5.5}$$

where h is a characteristic element size. For linear elements, one can show that this is equivalent to:

$$\left[\mathbf{M}_c + \lambda \left(\mathbf{M}_l - \mathbf{M}_c\right)\right] \boldsymbol{\alpha} = \mathbf{M}_{p1p0} \boldsymbol{\alpha}_0 \quad , \tag{5.6}$$

where $\mathbf{M}_l$ denotes the lumped mass matrix [28]. In the examples shown below this form of smoothing was used for the gradients, setting $\lambda = 0.05$.

6. Examples

All the numerical examples were carried out using two finite element codes. The first, FEELAST [29], is a finite element code based on simple linear (truss), triangular (plate) and tetrahedral (volume) elements with constant material properties per element that only solves the linear elasticity equations. The second, CALCULIX [30], is a general, open source finite element code for structural mechanical applications with many element types, material models and options. The optimization loops were steered via a simple shell-script for the adjoint-based optimization. In all cases, a 'target' distribution of $\alpha(\mathbf{x})$ was given, together with defined external forces $\mathbf{f}_\Gamma$. The problem was then solved, i.e. the displacements $\mathbf{u}(\mathbf{x})$ and strains $\mathbf{s}(\mathbf{x})$ were obtained and recorded at the 'measurement locations' $\mathbf{x}_j,\ j = 1, \mathrm{m}$. This then yielded the 'measurement pair' $\mathbf{f}, \mathbf{u}_j,\ j = 1, \mathrm{m}$ or $\mathbf{f}, \mathbf{s}_j,\ j = 1, \mathrm{m}$ that was used to determine the material strength distributions $\alpha(\mathbf{x})$ in the field.

The first cases serve to verify that the procedure can recover a uniform strength factor, starting for an arbitrary distribution. The subsequent cases treat the more realistic scenario of trying to determine regions of weakening materials. The element complexity and dimensionality also increases as the examples progress: the first cases are with truss elements, followed by cases with beam and plate elements, as well as plane stress and 3-D solids.

6.1. Crane

The case is shown in Fig. 6.1 and considers a typical crane used at construction sites. The crane has a height of $1,400$ cm, and the arm has a length of $2,500$ cm. A typical truss is about 100 cm long and has an area of 5 cm^2. Density, Young's modulus and Poisson rate were set to $\rho = 7.8$ gr/cm^3, $E = 2 \cdot 10^{12}$ gr/sec^2/cm, $\nu = 0.3$, respectively. The two end points on the arm had applied loads of $f_y = -2.0 \cdot 10^9$ gr cm/s^2, while the two end points on balancing/back part of the arm had loads of $f_y = -1.0 \cdot 10^9$ gr cm/s^2. The finite element discretization consisted of 350 linear truss elements. The loads lead to a displacement in the vertical direction $w_y = -18$ cm at the tip of the arm. The top Fig. 6.1 shows the strength factor α and the ten measuring points used (which in this case coincide with nodes of the finite element mesh), while the bottom figure displays the displacement field.

Displacement measurements

Given the desired/measured displacements at these 10 measuring points, different starting values for the strength factor α were explored. Recall that the target strength factor is $\alpha = 1$, uniformly in all trusses. If the procedure cannot recover this simple strength factor from any arbitrary initial distribution, its utility is doubtful. Figs. 6.2–6.4 show the results obtained when starting from a uniform value of $\alpha = 2.0$ without (Fig. 6.3(a)) and with (Fig. 6.3(b)) gradient smoothing. In each of these graphs in the upper half the vertical color bar corresponds to the absolute value of the difference between the target and actual displacements at the measuring points (in cm), and is denoted by 'Diff_Displ', while the horizontal color bar corresponds to the strength factor α_e in the element and is denoted by 'Strength'. The lower half shows the displacement field (in cm) and the corresponding color bar is denoted by 'Displ'. One can see that for this case gradient smoothing is essential: the case without smoothing achieves a fairly good reduction in the difference between the measured and computed displacements (Fig. 6.3(a)), but the strength factor distribution is very different from the target.

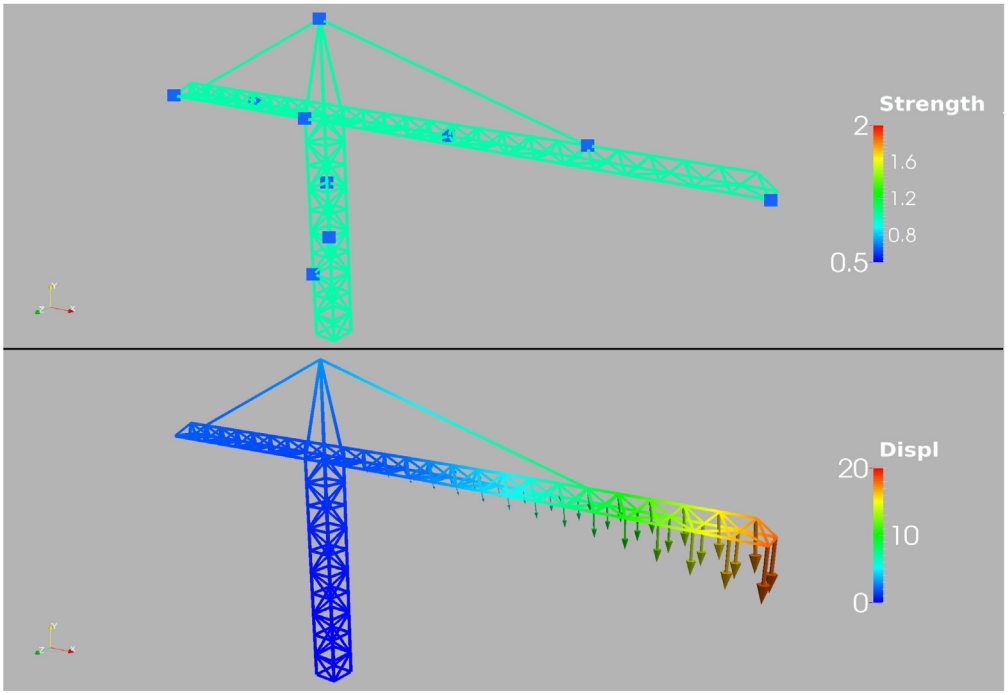

Fig. 6.1. Crane: base case ($\alpha = 1.0$) [Top: Measuring points and strength factor in the trusses; Bottom: Displacement field].

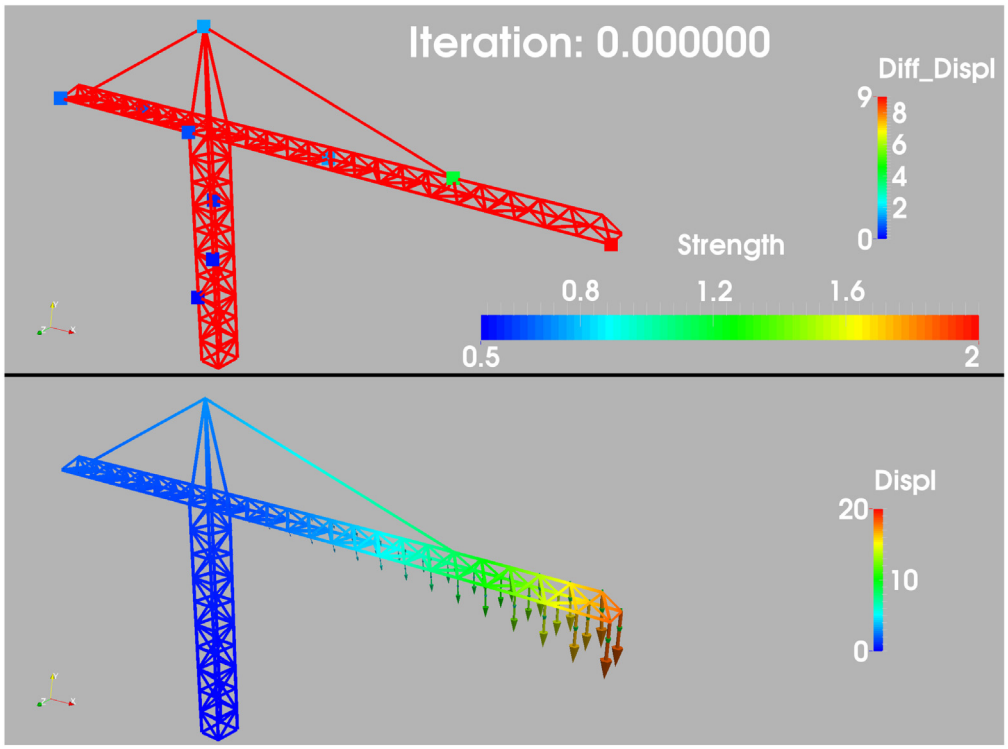

Fig. 6.2. Crane: Initial optimization iteration with initial strength factor $\alpha = 2.0$. *Top panel:* Strength factor in the trusses; *Bottom panel:* Displacement field. The vertical bar in top panel corresponds to the absolute value of the difference between the target and actual displacements at the measuring points (in *cm*), and is denoted by 'Diff_Displ', while the horizontal color bar corresponds to the strength factor α_e in the element and is denoted by 'Strength'. The bottom panel shows the displacement field (in *cm*) and corresponding colorbar is denoted by 'Displ'. (For interpretation of the references to color in this figure legend, the reader is referred to the web version of this article.)

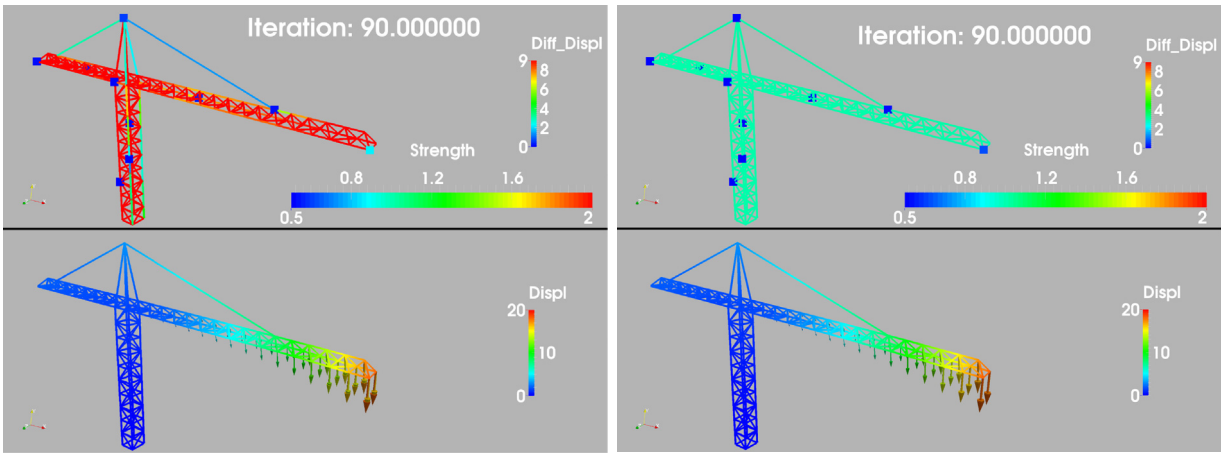

(a) Without smoothing (b) With smoothing

Fig. 6.3. Crane: 90-th optimization iteration with initial strength factor $\alpha = 2.0$. *Top panel:* Strength factors in the trusses; *Bottom panel:* Displacement fields. The vertical bar in top panel corresponds to the absolute value of the difference between the target and actual displacements at the measuring points (in *cm*), and is denoted by 'Diff_Displ', while the horizontal color bar corresponds to the strength factor α_e in the element and is denoted by 'Strength'. The bottom panel shows the displacement field (in *cm*) and corresponding colorbar is denoted by 'Displ'. Notice that left column corresponds to no smoothing and right one with smoothing. The latter produces correct results. (For interpretation of the references to color in this figure legend, the reader is referred to the web version of this article.)

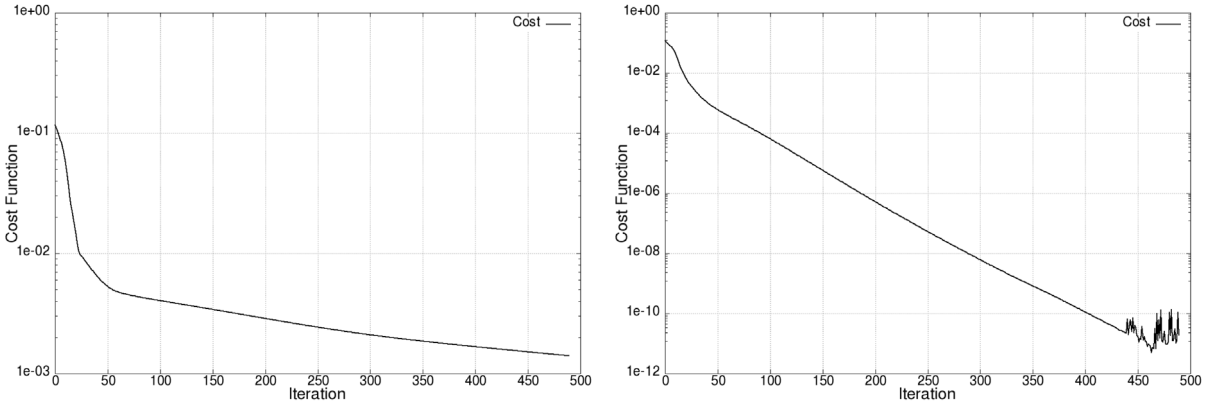

(a) Without smoothing (b) With smoothing

Fig. 6.4. Crane: Start: Random $\alpha = 2.0$, cost function history.

Fig. 6.4 shows the evolution of the cost function for optimizations with and without smoothing of gradients. It can be seen that without smoothing the optimization stalls around a local minimum, while the second case allows the objective function to reach the optimal solution.

Figs. 6.5 and 6.6 show the results obtained when starting from a random distribution of α without and with gradient smoothing. As before, one can see that for this case gradient smoothing is essential: the case without smoothing achieves a near-perfect match between the measured and computed displacements (Fig. 6.6(a)), but the strength factor distribution is very different from the target. This is also reflected in Fig. 6.7, where the evolution of the cost function is plotted for both cases.

Strain measurements

Ten strain measuring points were defined in trusses along the structure (see top left of Figs. 6.8 and 6.9). Given the desired/measured strains at these 10 measuring points, different starting values for the strength factor α were explored. The results obtained and behaviors observed were very similar to the cases with displacement measurements: gradient smoothing was essential. Therefore, in the sequel only results with gradient smoothing are shown. Figs. 6.8 and 6.9 show the results obtained when starting from a uniform value of $\alpha = 0.5$. The top figures show the actual values while the bottom part shows the expected strain and strength distribution in the trusses. Note also on the top left the differences in target and actual strain at the measurement points. The evolution of the cost function for this case is plotted in Fig. 6.10.

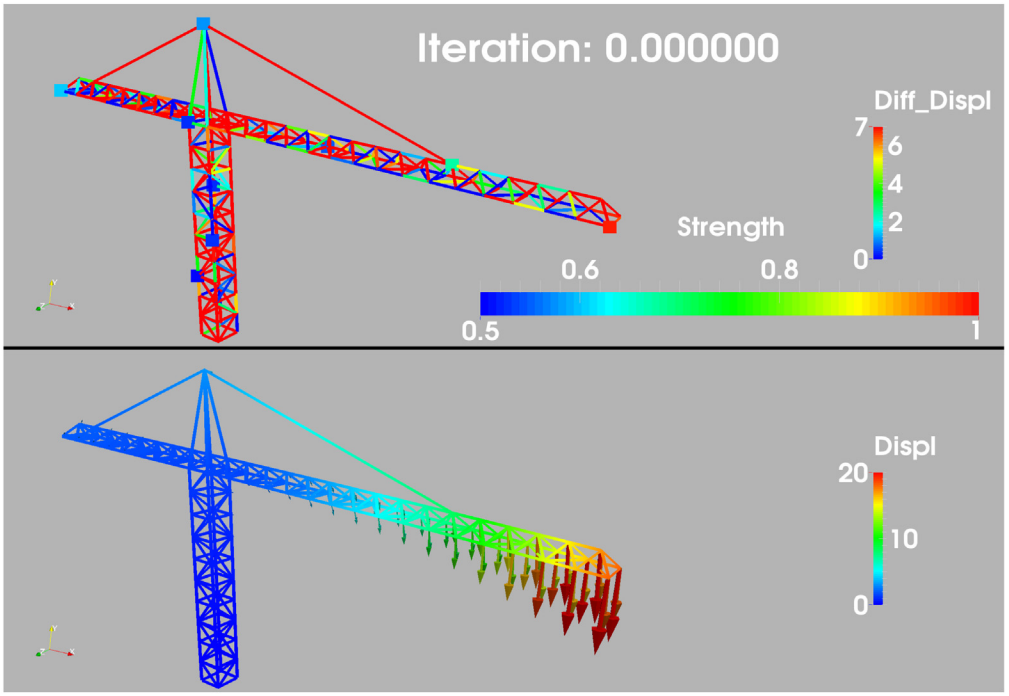

Fig. 6.5. Crane: Initial optimization iteration with random initial strength factor α. *Top panel:* Strength factor in the trusses; *Bottom panel:* Displacement field. The vertical bar in top panel corresponds to the absolute value of the difference between the target and actual displacements at the measuring points (in *cm*), and is denoted by 'Diff_Displ', while the horizontal color bar corresponds to the strength factor α_e in the element and is denoted by 'Strength'. The bottom panel shows the displacement field (in *cm*) and corresponding colorbar is denoted by 'Displ'. (For interpretation of the references to color in this figure legend, the reader is referred to the web version of this article.)

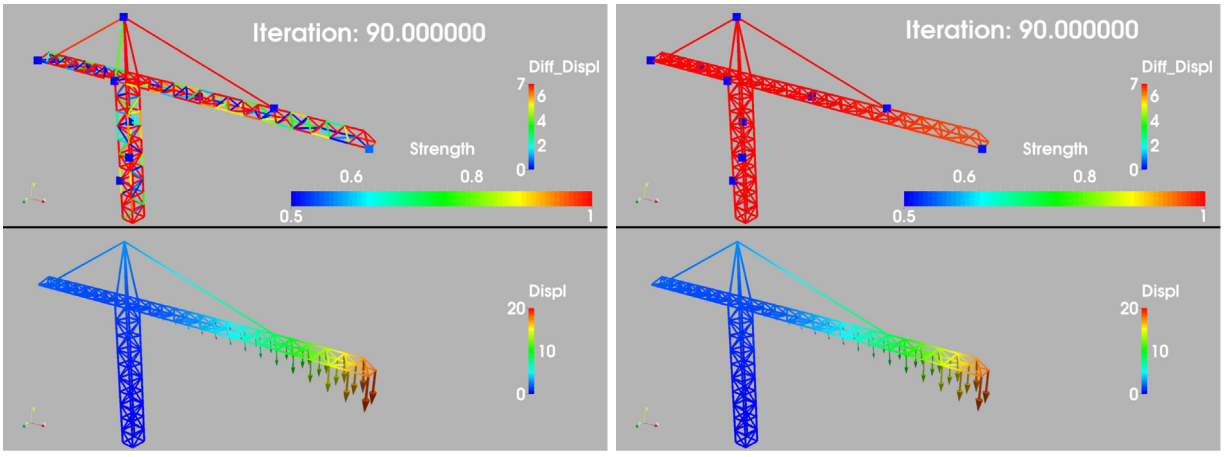

(a) Without smoothing (b) With smoothing

Fig. 6.6. Crane: 90-th optimization iteration with initial strength factor α being random. *Top panel:* Strength factors in the trusses; *Bottom panel:* Displacement fields. The vertical bar in top panel corresponds to the absolute value of the difference between the target and actual displacements at the measuring points (in *cm*), and is denoted by 'Diff_Displ', while the horizontal color bar corresponds to the strength factor α_e in the element and is denoted by 'Strength'. The bottom panel shows the displacement field (in *cm*) and corresponding colorbar is denoted by 'Displ'. Notice that left column corresponds to no smoothing and right one with smoothing. The latter produces correct results. (For interpretation of the references to color in this figure legend, the reader is referred to the web version of this article.)

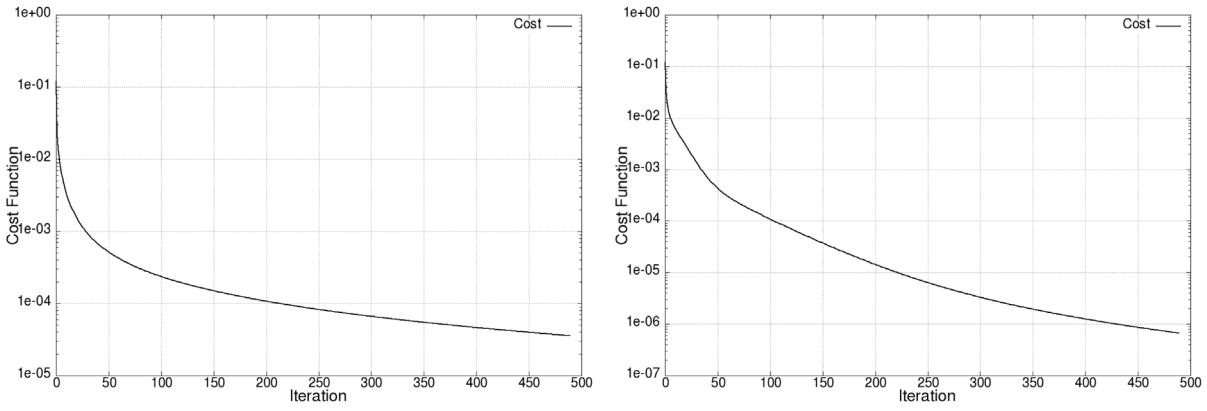

(a) Without smoothing (b) With smoothing

Fig. 6.7. Crane: Start: Random α, cost function history.

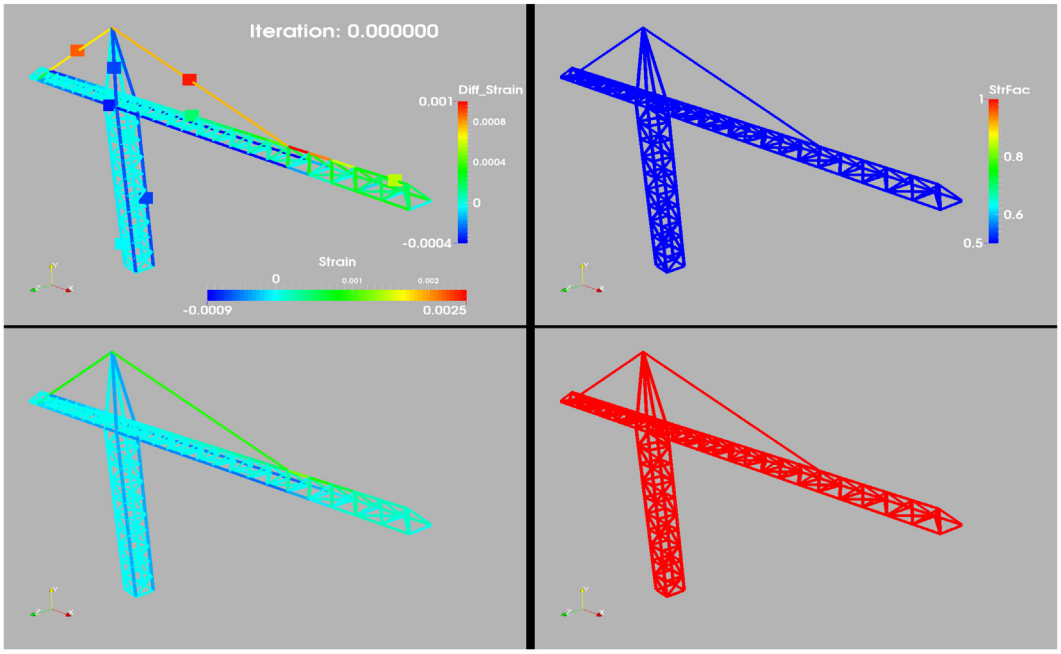

Fig. 6.8. Crane: Start: $\alpha = 0.5$, Iteration: 0 [Top left: Stress in the trusses; difference of measured/current strains; Top right: Strength factor in the trusses; Bottom left: Target stress in the trusses; Bottom right: Target strength factor in the trusses].

Figs. 6.11 and 6.12 show the results obtained when starting from a uniform value of $\alpha = 1.0$ for the case that the lower part of the crane tower has been weakened to $\alpha = 0.5$. As before, the top figures show the actual values while the bottom part shows the expected strain and strength distribution in the trusses. The convergence of the cost function is shown in Fig. 6.13.

Displacement measurements with multiple loads

The same 'weakened bottom' scenario was also computed for the 10 displacement measurement points shown before, but with 3 load scenarios. The first is the same as before, the second induces a torsion of the mast and the third applies forces between the mast and the end of the arm. Figs. 6.14 and 6.15 show the results obtained when starting from a uniform value of $\alpha = 1.0$. In the figures, the top left shows the computed strength factor, the top right the desired (exact) strength factor, while the bottom shows the displacements (computed and desired overlapped) for the 3 load cases. Fig. 6.16 shows how the cost functions for all three load cases go down with iterations. The objective function used for this optimization case is the sum of those quantities.

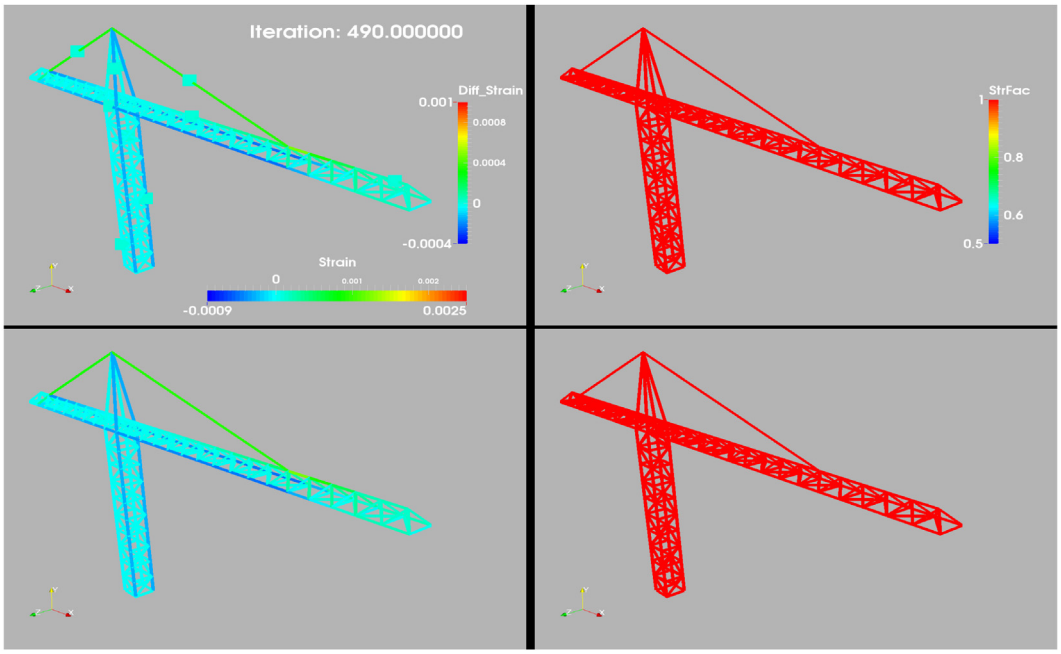

Fig. 6.9. Crane: Start: $\alpha = 0.5$, Iteration: 490 [Top left: Stress in the trusses; difference of measured/current strains; Top right: Strength factor in the trusses; Bottom left: Target stress in the trusses; Bottom right: Target strength factor in the trusses].

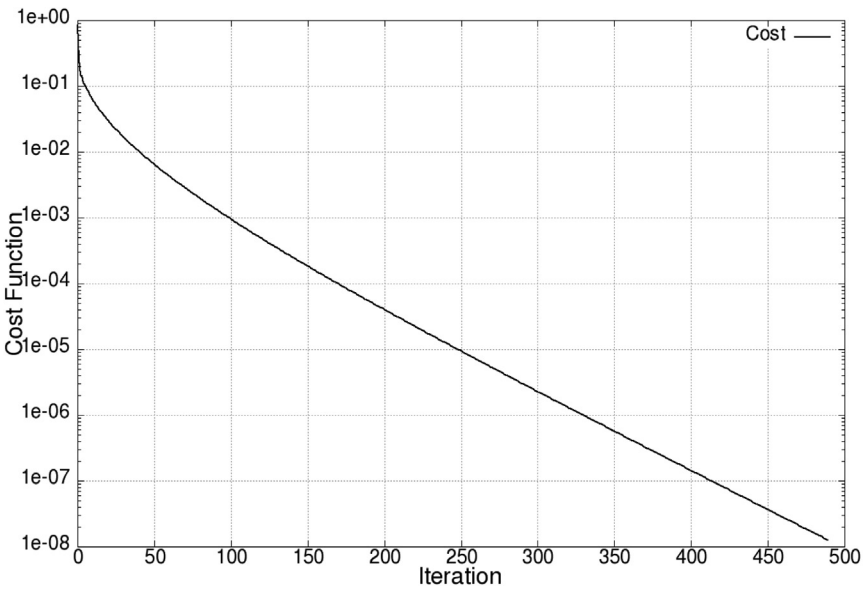

Fig. 6.10. Crane: Start: $\alpha = 0.5$, cost function for the strain measured case.

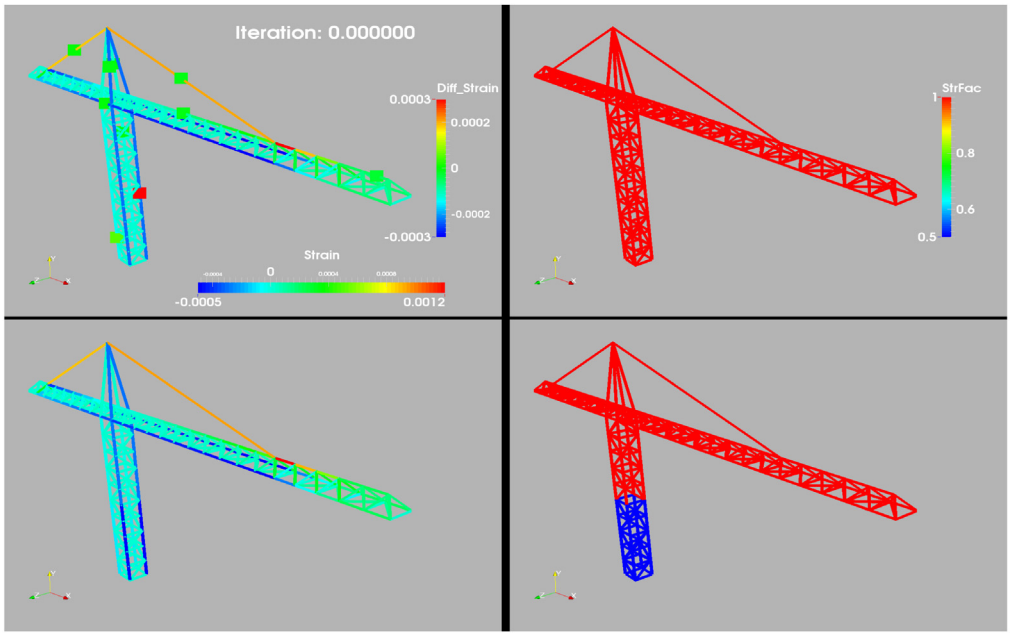

Fig. 6.11. Weakened Crane: Start: $\alpha = 1.0$, Iteration: 0 [Top left: Stress in the trusses; difference of measured/current strains; Top right: Strength factor in the trusses; Bottom left: Target stress in the trusses; Bottom right: Target strength factor in the trusses].

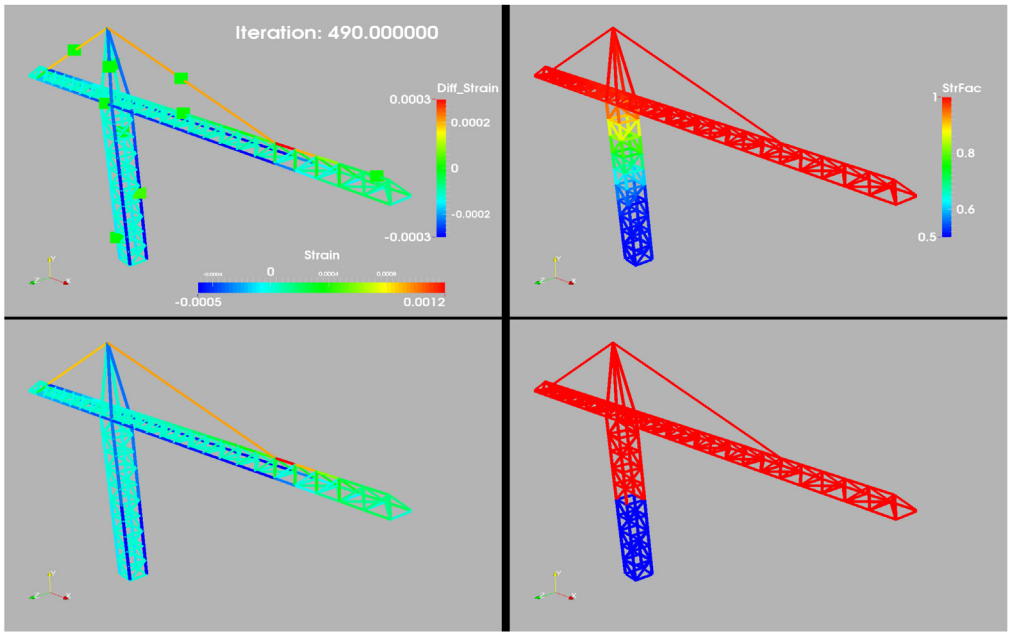

Fig. 6.12. Weakened Crane: Start: $\alpha = 1.0$, Iteration: 490; [Top left: Stress in the trusses; difference of measured/current strains; Top right: Strength factor in the trusses; Bottom left: Target stress in the trusses; Bottom right: Target strength factor in the trusses].

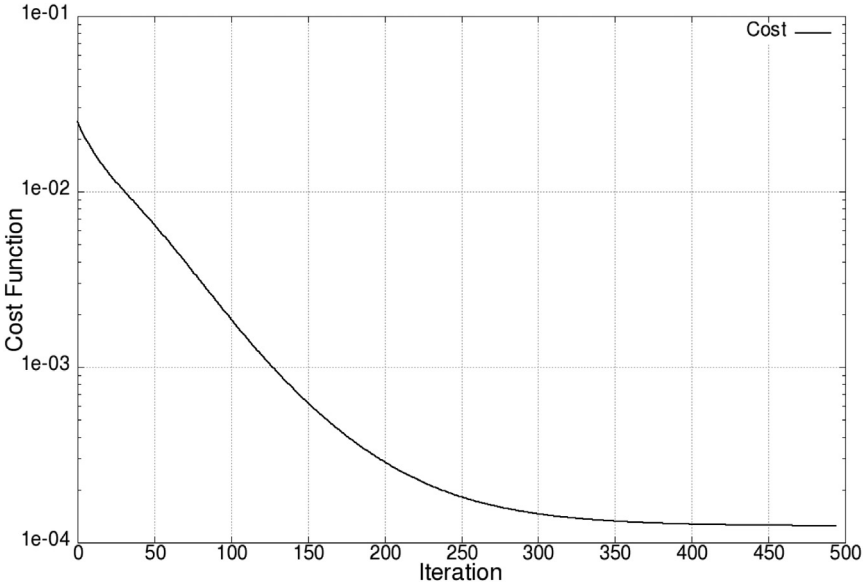

Fig. 6.13. Crane: Start: $\alpha = 1.0$, cost function for the strain measured case with weakened bottom.

Table 6.1
Footbridge: Components.

Component #	Shape. Dimensions in mm
1	Steel plate. $t = 10$
2	Steel beam. Hollow section $300 \times 200 \times 12$
3	Steel beam. Hollow section $200 \times 200 \times 10$
4	Steel beam. Hollow section $180 \times 180 \times 10$
5	Steel beam. Hollow section $180 \times 180 \times 5$
6	Steel beam. Hollow section $200 \times 200 \times 10$
7	Steel beam. Hollow section $200 \times 100 \times 5$

6.2. Footbridge

This case considers a typical footbridge and was taken from [31]. The different types of trusses and plates whose dimensions have been compiled in Table 6.1, can be discerned from Fig. 6.17. Density, Young's modulus and Poisson ratio were set to $\rho = 7800\ \mathrm{kg/m^3}, E = 2 \cdot 10^{11}\ \mathrm{kg/sec^2/m}, \nu = 0.3$ respectively. The structure was modeled using 136 shell and 329 beam elements. The bridge is under a distributed load of 1 MPa in the downwards direction, applied to every plate, as well as gravity.

Fig. 6.18 shows the target case where one beam in the structure has been weakened to $\alpha = 0.1$. In 6.18(a), the location of the 8 sensors is shown, along with the target displacements. Starting from a uniform value of $\alpha = 1.0$, shown in Fig. 6.19, the target case is nearly reproduced in 200 steepest descent iterations, as can be seen in Fig. 6.20. Fig. 6.20(a) shows the displacement field (in m) with the label on the bottom right and the magnitude of the difference between target and actual displacements at the measuring points (in m) with the label at the upper left. Fig. 6.20(b) shows the strength factor in the elements. The evolution of the objective function is shown in Fig. 6.21. The optimizer is able to locate the weakened beam. The evolution of objective with respect to optimization iteration appears smooth.

This case highlights the possibility of working with multiple element types with no extra difficulties. However, it has been verified that in order to find weak spots in shell elements ones needs a larger number of sensors.

6.3. Plate with hole

The case is shown in Figs. 6.22–6.24 and considers a plate with a hole. The plate dimensions (in meters) are $0 \leq x \leq 60$, $0 \leq y \leq 30$, $0 \leq z \leq 0.1$. A hole of diameter $d = 10$ is placed in the middle ($x = 30, y = 15$). Density, Young's modulus and Poisson rate were set to $\rho = 7800\ \mathrm{kg/m^3}, E = 2 \cdot 10^{11}\ \mathrm{kg/sec^2/m}, \nu = 0.3$, respectively. 672 linear, triangular, plain stress elements were used.

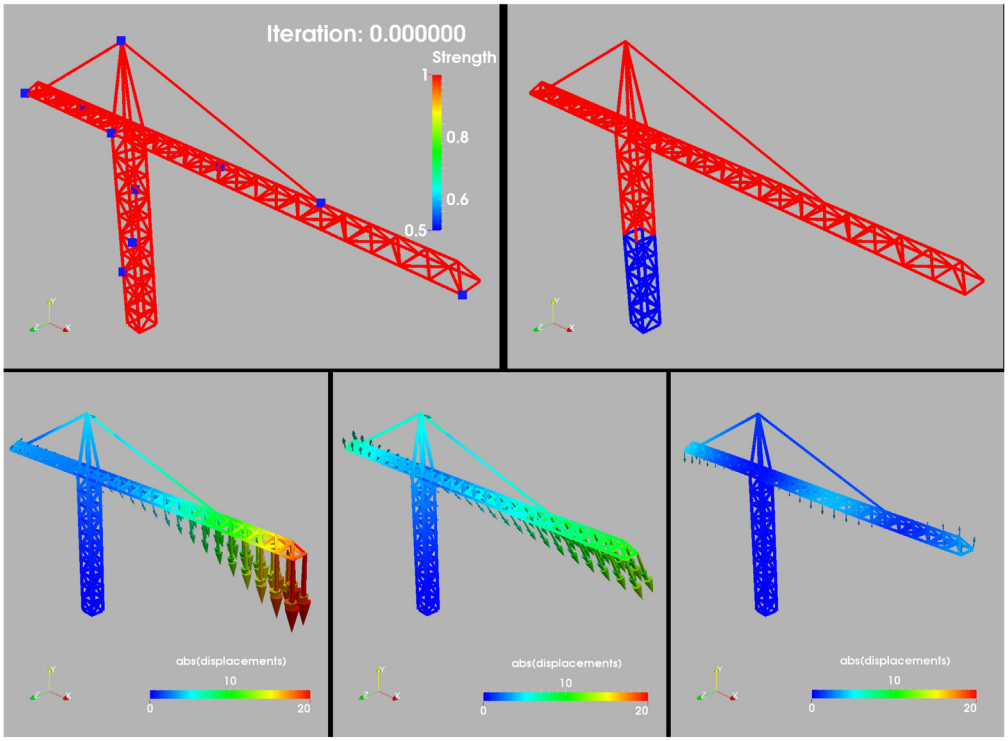

Fig. 6.14. Weakened Crane: Start: $\alpha = 1.0$, Iteration: 0 [Top left: Strength factor in the trusses; Top right: Target strength factor in the trusses; Bottom left–right: Displacement fields (target and current) for load cases 1–3].

The left boundary of the plate is assumed clamped ($\mathbf{u} = 0$), while a horizontal line load of $q_x = 10^5$ kg/sec^2 was prescribed at the right end. The left part of the figures show the computed strength factor and displacements (in m), while the right part displays the expected values (the strength factor range is $0.1 \leq \alpha \leq 1$). The 14 measurement points, together with the differences in displacements between measured and computed values (in m) are also shown in the bottom right part. Fig. 6.24 shows the evolution of the cost function.

As can be seen in the graph, the optimum solution is reached within 100 iterations. Furthermore, the weakened portion is very accurately identified (Fig. 6.23).

6.4. L-shape

The case, taken from [16] is shown in Figs. 6.25 and 6.26 and considers an L-shaped block subjected to a vertical force. The plate dimensions are (in meters): $0 \leq x \leq 0.6$, $0 \leq y \leq 1.3$, $0 \leq z \leq 0.30$. The upper part extends up to $x = 0.45$, and the L-part extends to $y = 0.3$. A fillet with radius $r = 0.05$ was added to avoid extreme stress concentrations. Density, Young's modulus and Poisson rate were set to $\rho = 7800$ kg/m^2, $E = 2 \cdot 10^{11}$ kg/sec^2/m, $\nu = 0.3$, respectively. 14,622 linear, tetrahedral elements were used. The top boundary of the block is assumed clamped ($\mathbf{u} = 0$), while a vertical surface load of $f_y = -2 \cdot 10^7$ kg/sec^2/m was prescribed at the top of the L-shaped region (only the straight section, i.e. not the fillet).

The 10 visible measurement points (the other 10 are at the same x, y positions but on the other z-face), together with the target displacements and strength factors are shown in Figs. 6.25(a)–(b) (the strength factor range again is $0.1 \leq \alpha \leq 1$). This case was particularly challenging because the weakened region does not have a considerable influence on the displacements. Therefore, many possible strength factor distributions can yield similar displacements. The smoothing of the gradient was a key tool for the optimizer to arrive at the proper solution.

Figs. 6.25(c)–(d) show the initial conditions for the optimization loop. The results obtained after 100 steepest descent iterations are displayed in Fig. 6.26 for multiple runs with different passes of gradient smoothing. Note that for $n_{\text{smooth}} < 3$ the optimizer is not able to arrive to a useful solution. Fig. 6.26(d) shows an optimized state that is almost satisfactory, but not sufficiently refined. For the cases of $n_{\text{smooth}} = 4$ and $n_{\text{smooth}} = 5$, Figs. 6.26(e)–(f) show a clearly accurate representation of the weakened area. The objective history is shown in Fig. 6.27 for all cases. We observe a fast convergence for larger number of smoothing passes.

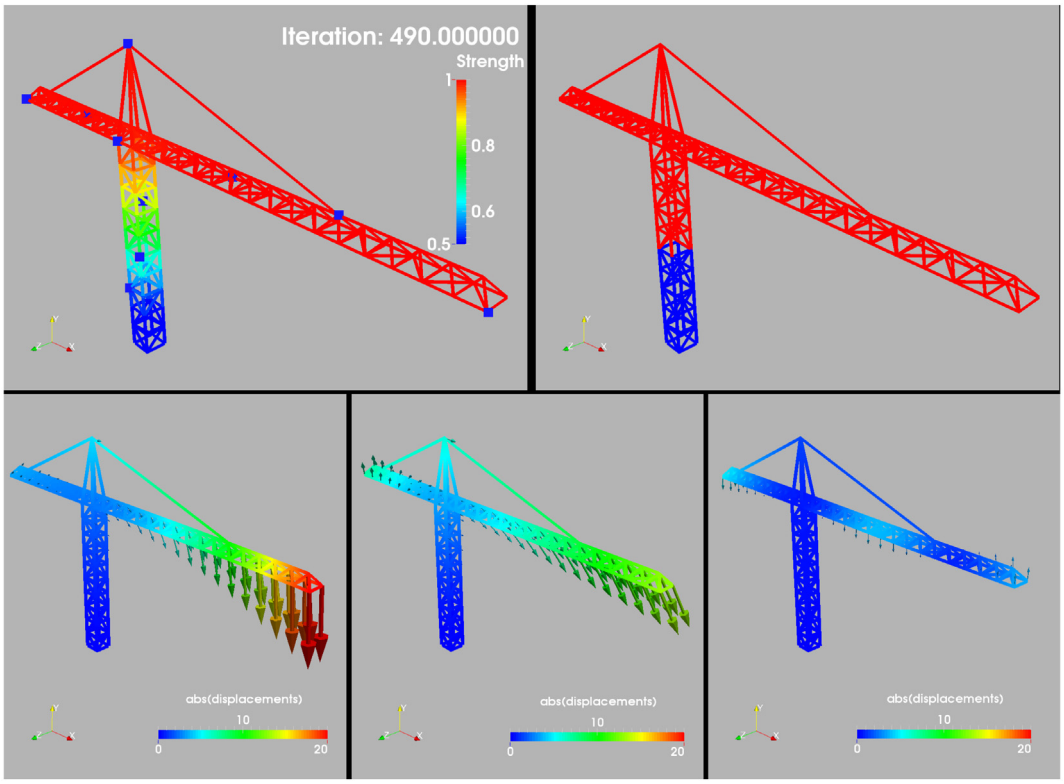

Fig. 6.15. Weakened Crane: Start: $\alpha = 1.0$, Iteration: 490 [Top left: Strength factor in the trusses; Top right: Target strength factor in the trusses; Bottom left–right: Displacement fields (target and current) for load cases 1–3].

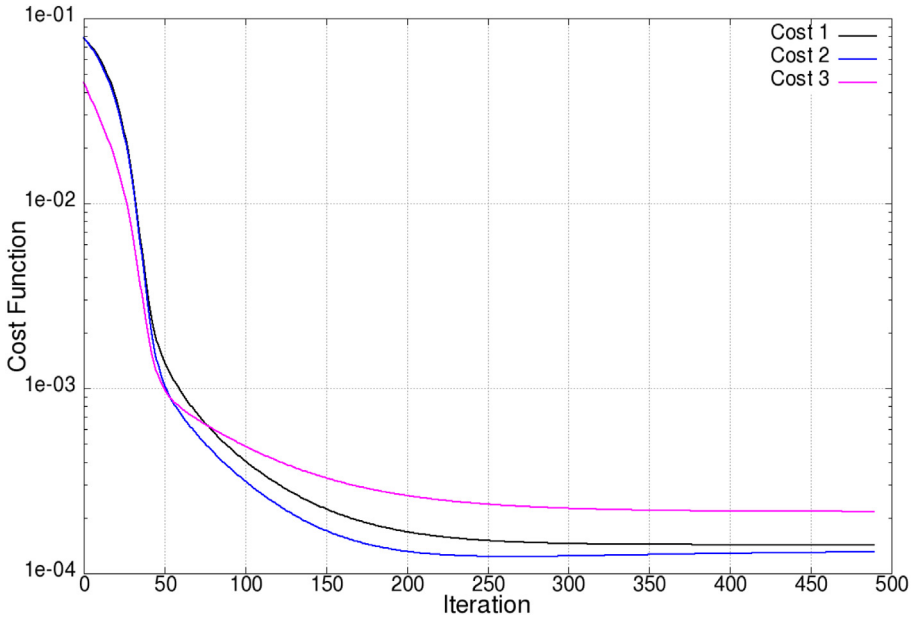

Fig. 6.16. Weakened Crane: Convergence history for the load cases.

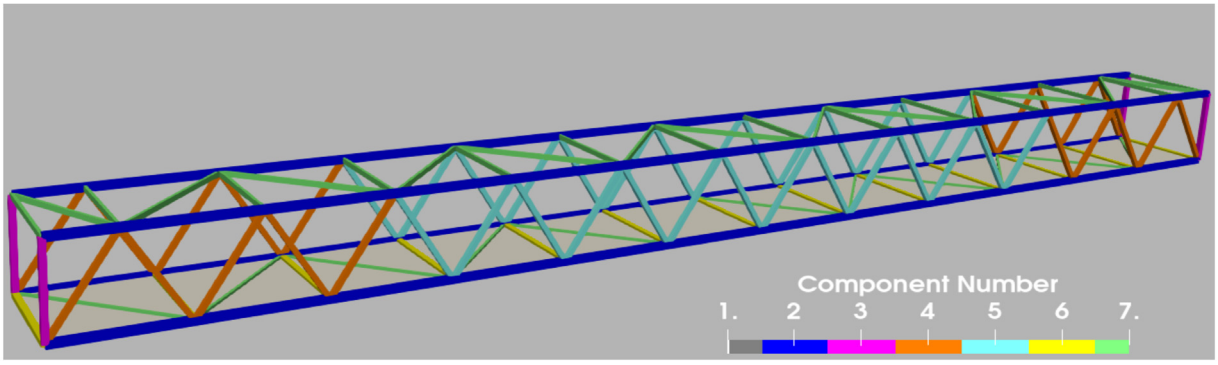

Fig. 6.17. Footbridge: Components.

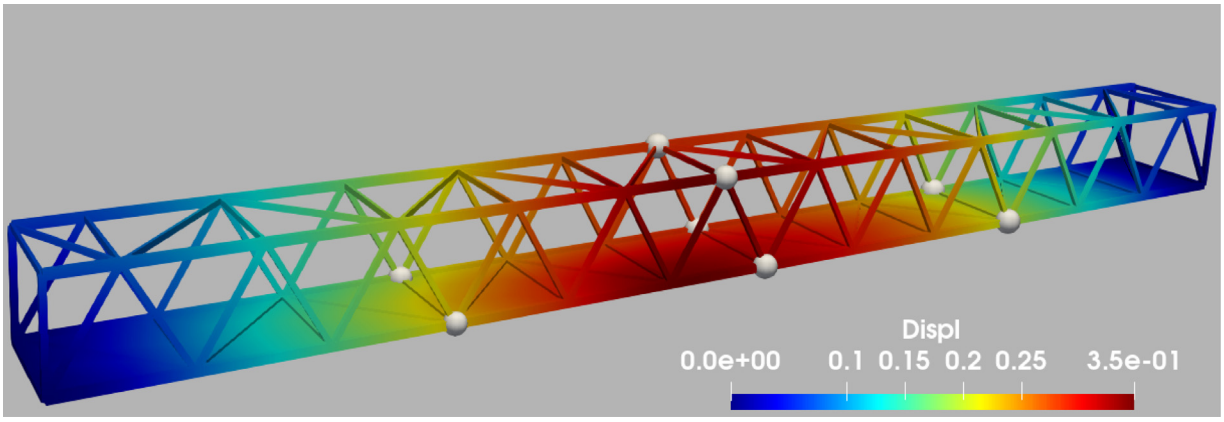

(a) Target Displacements and Sensor Locations

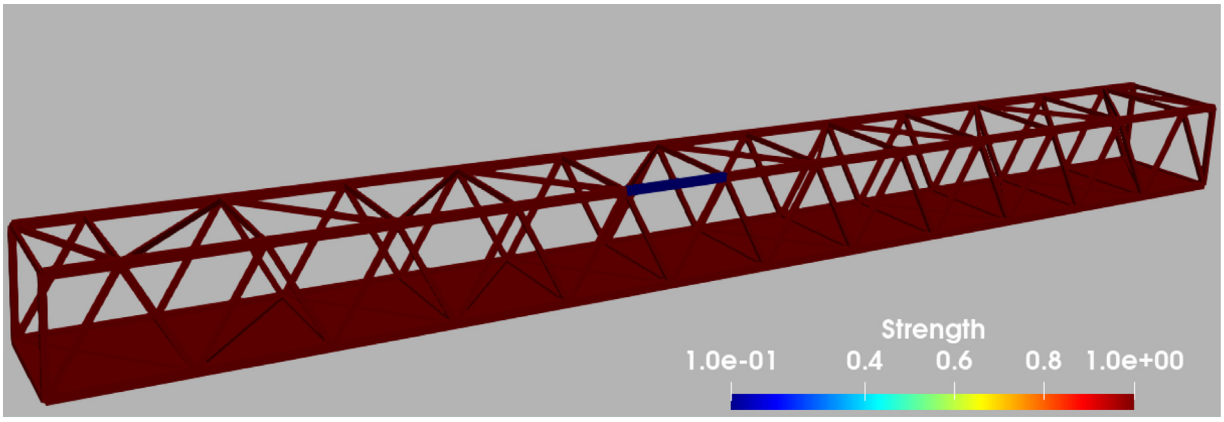

(b) Target Strength Factor

Fig. 6.18. Footbridge: Target Conditions. The color bars at the bottom right correspond to the actual displacements and strength factors, respectively. (For interpretation of the references to color in this figure legend, the reader is referred to the web version of this article.)

7. Conclusions and outlook

An adjoint-based procedure to determine weaknesses, or, more generally the material properties of structures has been presented. Given a series of force and displacement/strain measurements, the material properties are obtained by minimizing the adequately weighted differences between the measured and computed values. The approach is directly based on the finite element model of the structure of interest, which can be arbitrarily complex and be composed out of any kind of element formulation and combinations

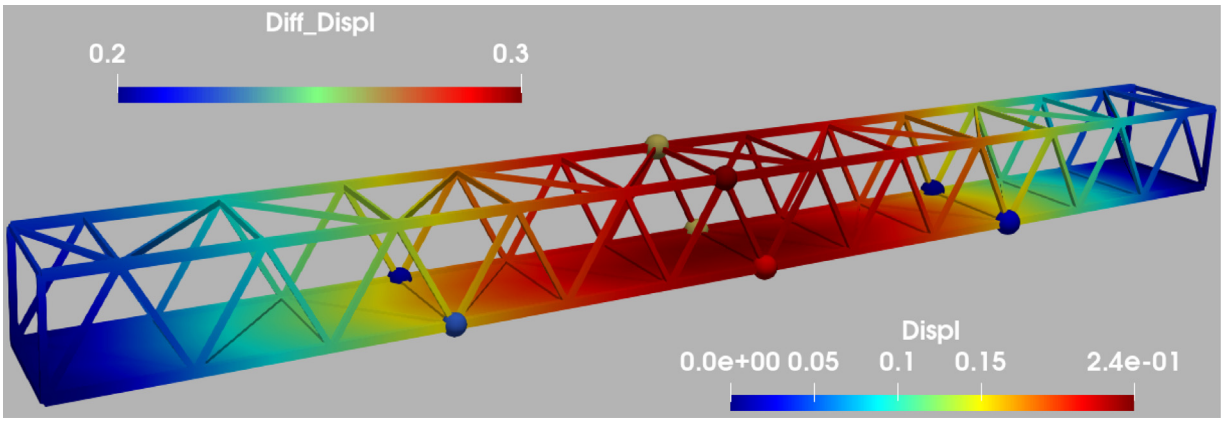

(a) Initial Displacements and Sensor Values

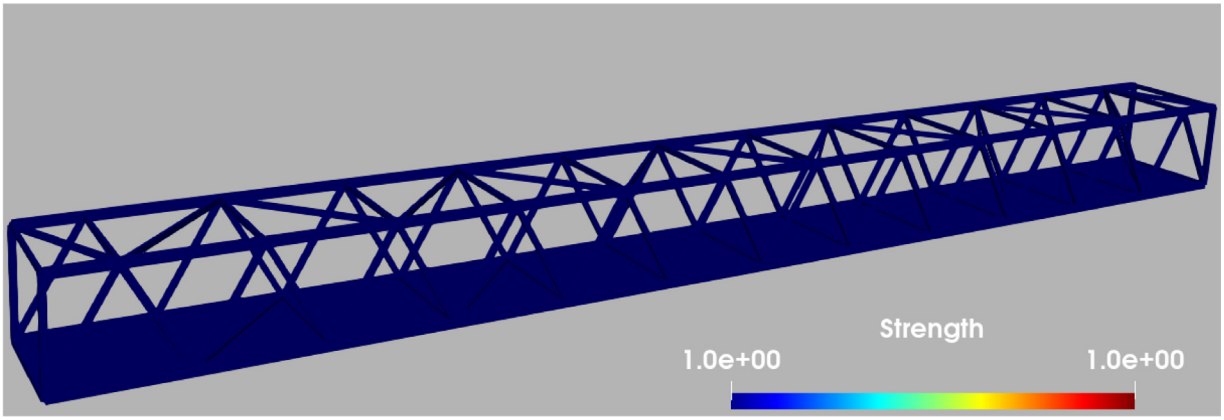

(b) Initial Strength Factor

Fig. 6.19. Footbridge: Initial optimization iteration. Figure (a) shows the displacements and (b) corresponds to the strength factor. The color bar on top left displays the magnitude of the difference between target and actual displacements at the measuring points (in m). Moreover, the color bars at the bottom right correspond to the actual displacements and strength factors, respectively. (For interpretation of the references to color in this figure legend, the reader is referred to the web version of this article.)

thereof. This is especially advantageous in complicated real-world applications. As a consequence, the procedure can provide highly resolved parameter distributions within the structure and allows for the localization of e.g. damage regions or other zones with deviations from the planned configuration.

It was found that in order to obtain reliable, convergent results the gradient of the cost function has to be smoothed.

Several examples are included that show the viability, accuracy and efficiency of the proposed methodology using both displacement and strain measurements for different types of elements and settings.

We consider this a first step that demonstrates the viability of the proposed adjoint-based methodology for system identification and its use for digital twins [26,27]. Many questions remain open, of which we just mention two obvious ones:

- What sensor resolution is required to obtain reliable results?
- Will these techniques work under uncertain measurements? [32,33].

Furthermore, the steepest descent procedures may be improved by going to a quasi or full Newton solver. But: will they be faster?

The answers to these questions are currently under investigation as well as further methodological details and application fields of this novel “twinning” strategy.

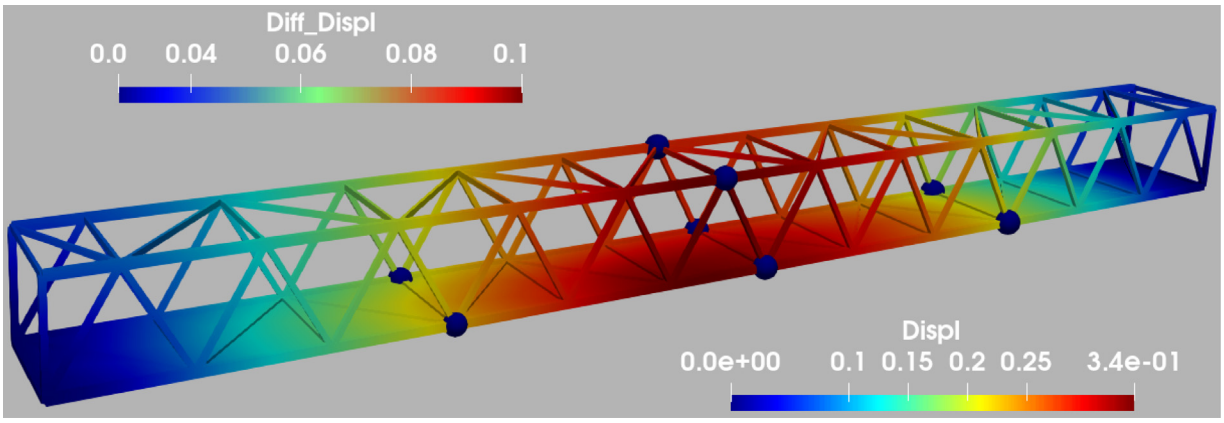

(a) Displacements Obtained

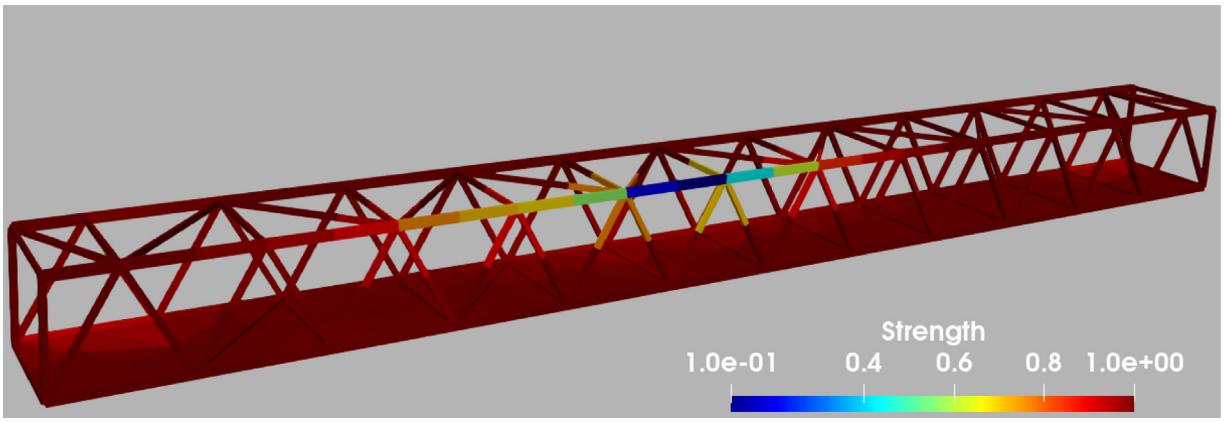

(b) Strength Factor Obtained

Fig. 6.20. Footbridge: Solution obtained at the 200-th optimization iteration. The upper panel shows the displacements and the lower one corresponds to the strength factor. The color bar on top left displays the magnitude of the difference between target and actual displacements at the measuring points (in m). Moreover, the color bars at the bottom right correspond to the actual displacements and strength factors. We observe that our optimization approach is able to identify the weakened beam. (For interpretation of the references to color in this figure legend, the reader is referred to the web version of this article.)

Declaration of competing interest

The authors declare that they have no known competing financial interests or personal relationships that could have appeared to influence the work reported in this paper.

Data availability

No data was used for the research described in the article.

Acknowledgments

This work is partially supported by NSF, United States grant DMS-2110263 and the AirForce Office of Scientific Research under Award NO: FA9550-22-1-0248.

Appendix. An explanation for smoothing

Below, we provide one explanation for smoothing (for instance, (5.3)) with the help of a continuous form of the optimization problem with elasticity equation as constraints. The main idea is that the discrete form of the gradient of the objective function must respect the continuous form. In other words, it is critical to construct structure preserving discretizations.

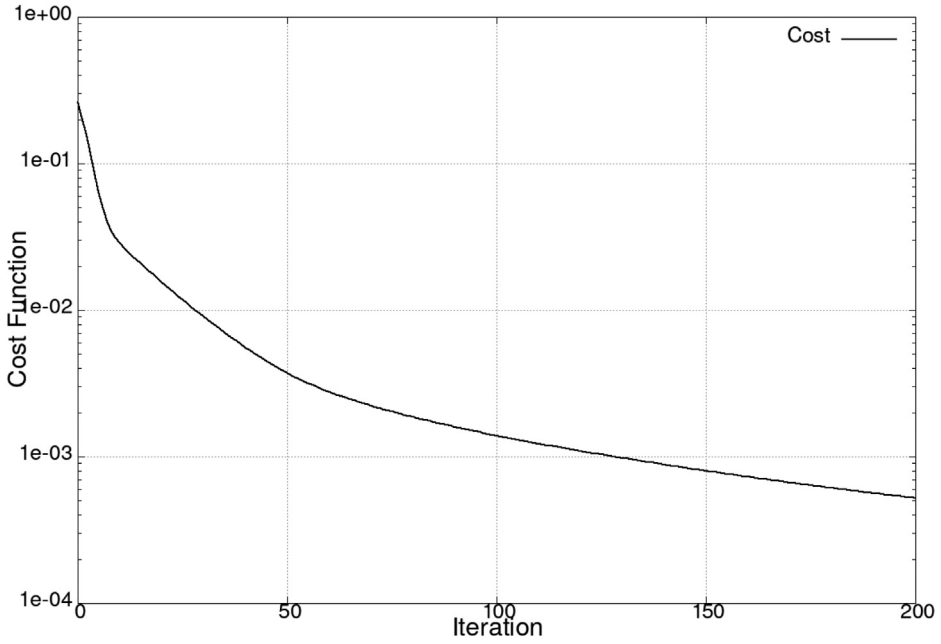

Fig. 6.21. Footbridge: Objective function history.

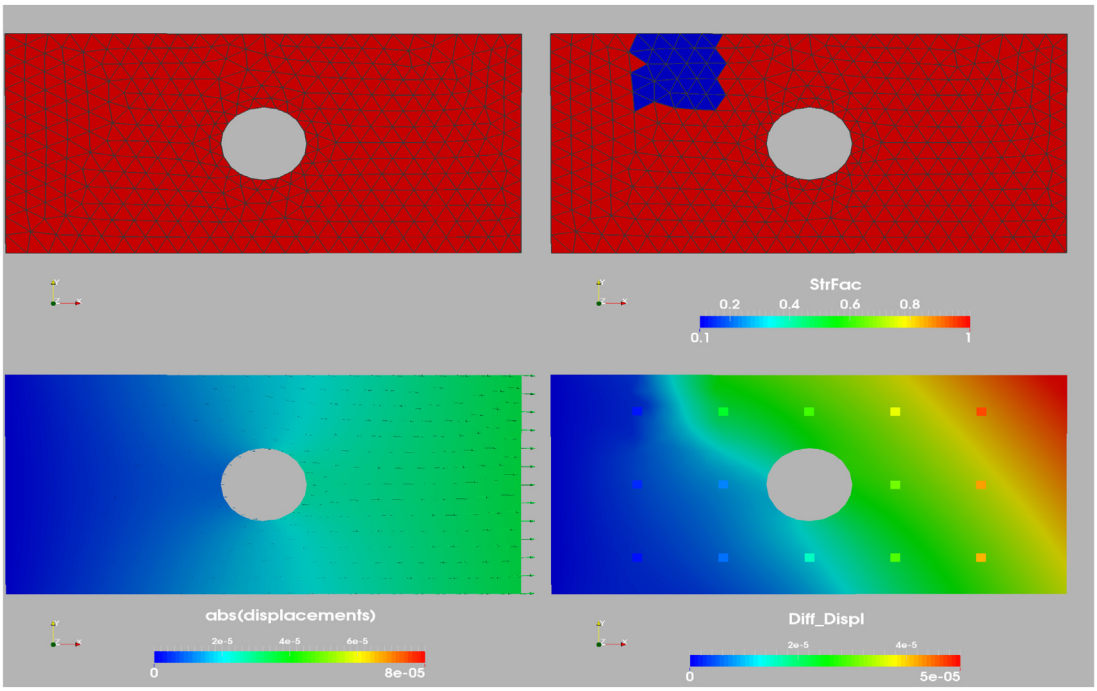

Fig. 6.22. Plate with hole: Start: $\alpha = 1.0$, Iteration: 0 [Top left: Strength factor; Top right: Target strength factor; Lower left: Displacement field; Lower right: Target displacement field and difference target/current at measurement points].

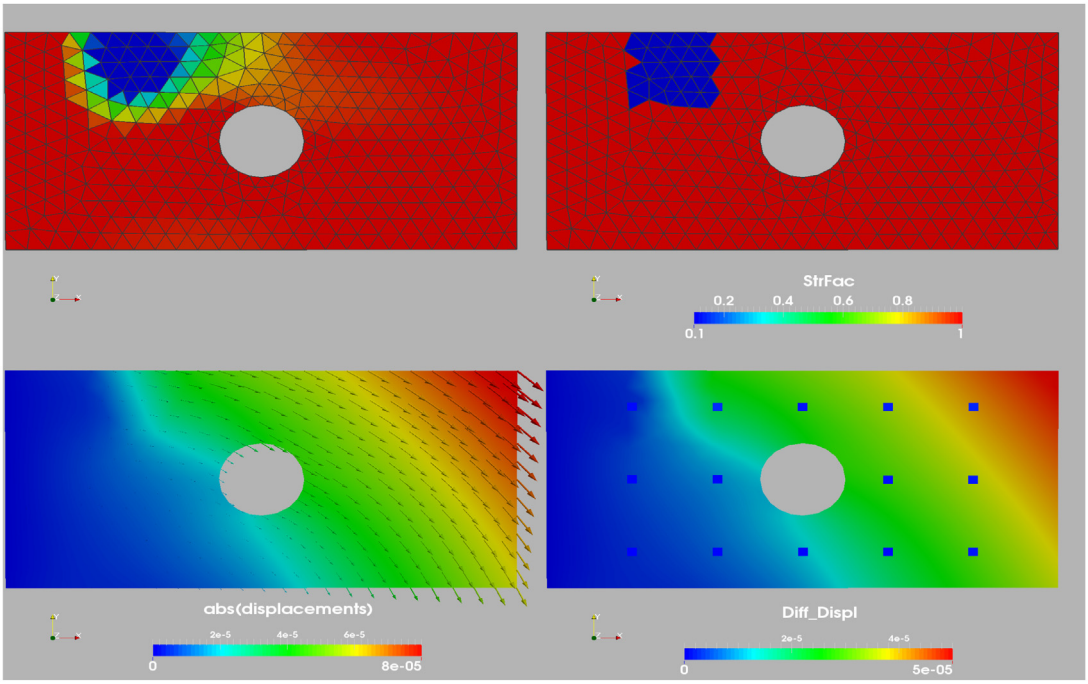

Fig. 6.23. Plate with hole: Start: $\alpha = 1.0$, Iteration: 89 [Top left: Strength factor; Top right: Target strength factor; Lower left: Displacement field; Lower right: Target displacement field and difference target/current at measurement points].

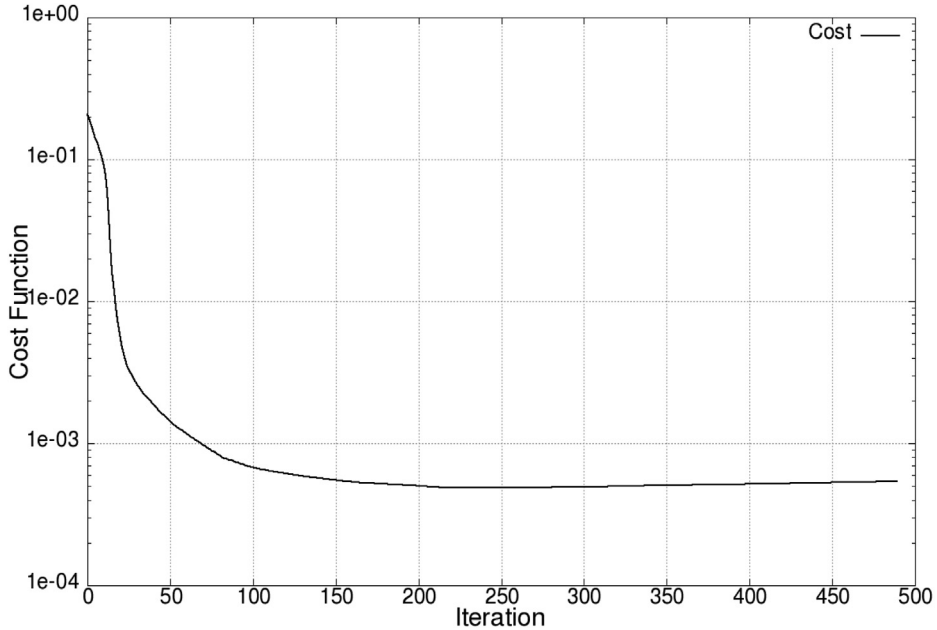

Fig. 6.24. Plate with hole: Cost function history.

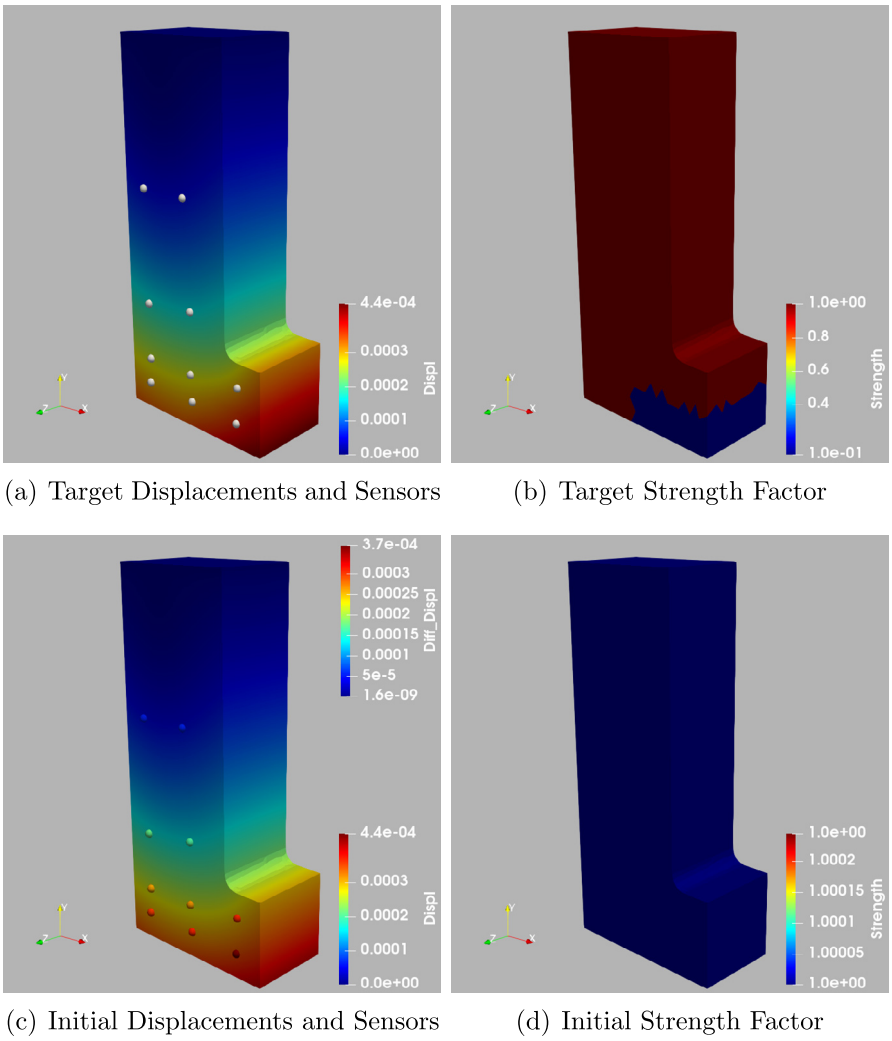

(a) Target Displacements and Sensors (b) Target Strength Factor

(c) Initial Displacements and Sensors (d) Initial Strength Factor

Fig. 6.25. L-Shape: Target and initial conditions.

Let Ω be a bounded open domain with boundary Γ. Let the boundary be divided into Γ_D (Dirichlet) and Γ_N (Neumann). Let $\boldsymbol{H}^1(\Omega;\Gamma_D)$ be the Sobolev space of vector valued functions which vanishes on Γ_D and $H^1(\Omega)$ be the usual Sobolev space for scalars. Consider the optimization problem:

$$\min_{(\boldsymbol{u},\alpha)\in\boldsymbol{H}^1(\Omega;\Gamma_D)\times\in H^1(\Omega)} I(\boldsymbol{u},\alpha) \tag{A.1a}$$

subject to PDE constraints

$$\begin{aligned} -\mathrm{div}(\boldsymbol{\sigma}(\boldsymbol{u};\alpha)) &= \boldsymbol{f} \quad \text{in } \Omega \\ \boldsymbol{u} &= \boldsymbol{0} \quad \text{on } \Gamma_D \\ \boldsymbol{\sigma}(\boldsymbol{u};\alpha)\boldsymbol{\nu} &= \boldsymbol{0} \quad \text{on } \Gamma_N\,, \end{aligned} \tag{A.1b}$$

where $\boldsymbol{\sigma}$ is the stress tensor and $\boldsymbol{f}$ is the given load.

Consider the PDE solution map $S : H^1(\Omega) \to \boldsymbol{H}^1(\Omega;\Gamma_D)$ such that $\alpha \mapsto S(\alpha) =: \boldsymbol{u}$ solves (A.1b). Then, we can write the reduced version of the minimization problem (A.1a) by eliminating the PDE constraints (A.1b)

$$\min_{\alpha\in H^1(\Omega)} \{J(\alpha) := I(S(\alpha),\alpha)\} \tag{A.2}$$

i.e., the reduced minimization problem (A.2) only depends on α. Since,

$$J : H^1(\Omega) \to \mathbb{R}, \quad \alpha \mapsto J(\alpha)$$

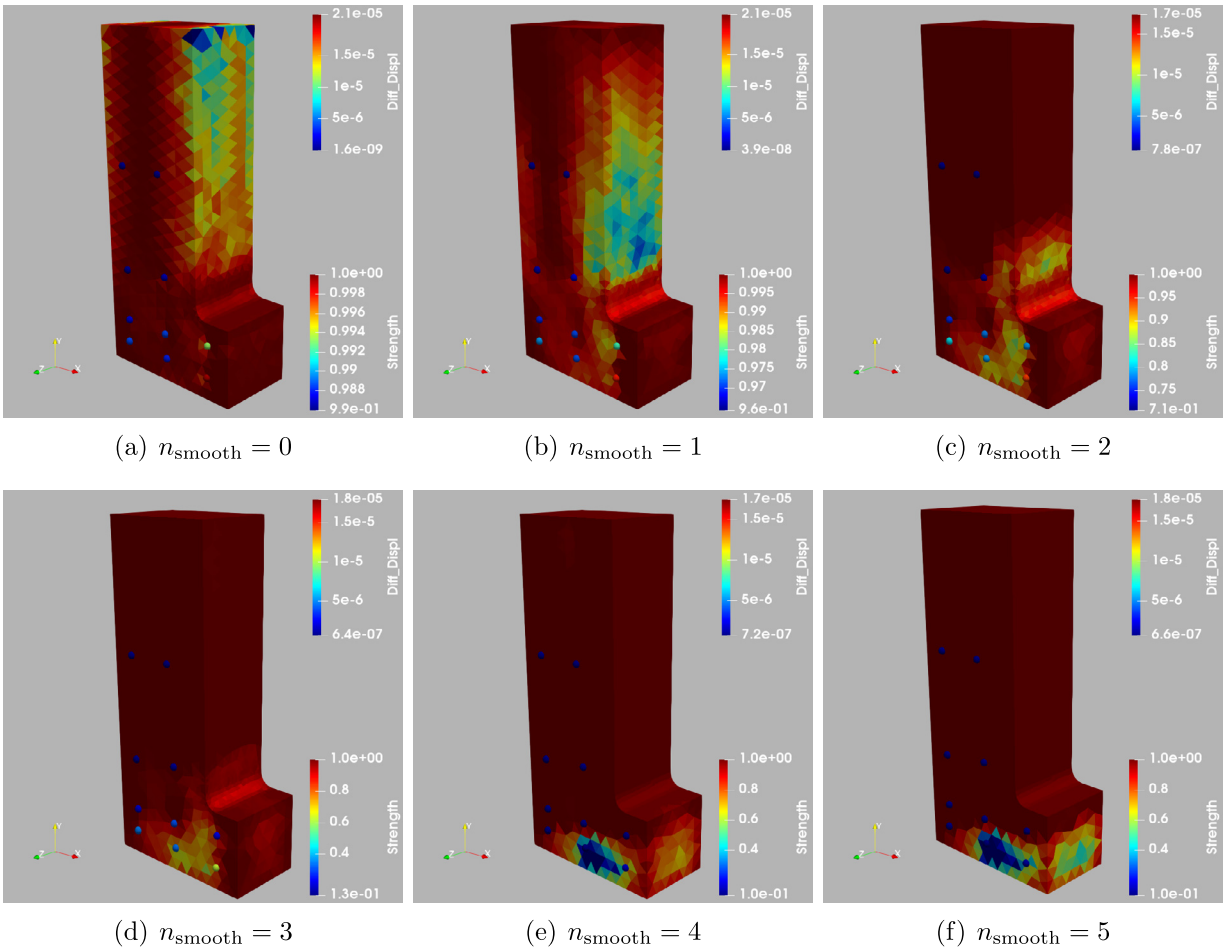

Fig. 6.26. L-Shape: Obtained strength factors for different passes of smoothing.

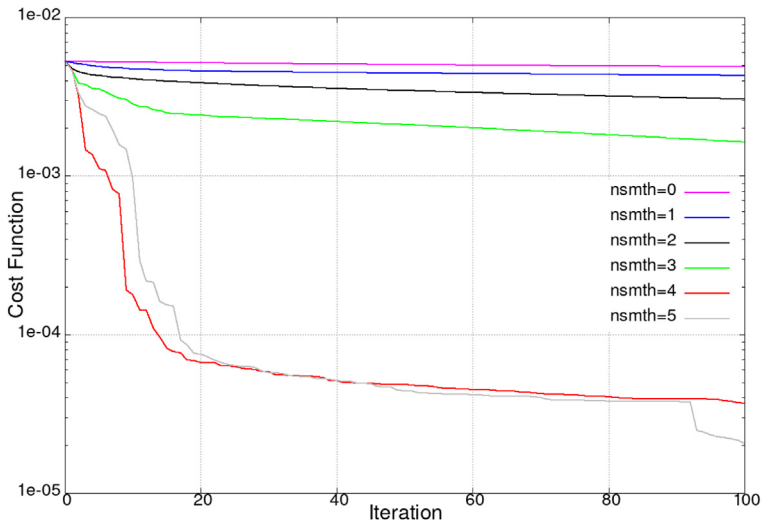

Fig. 6.27. L-Shape: Objective function history for different passes of smoothing.

therefore for $\alpha \in H^1(\Omega)$, we have that the directional derivative [22]

$$J'(\alpha) \in H^1(\Omega)^*$$

where $H^1(\Omega)^*$ is the dual space of $H^1(\Omega)$. Notice that $J'(\alpha)$ is precisely the directional derivative of the Lagrangian with respect to α. To obtain the correct expression of the gradient in the primal space $H^1(\Omega)$ we introduce the "Riesz map", solving the following Neumann problem

$$\begin{aligned} -\lambda\nabla^2\tilde{\alpha} + \tilde{\alpha} &= J'(\alpha) \quad \text{in } \Omega, \\ \nabla\tilde{\alpha}\cdot\boldsymbol{n} &= 0 \quad \text{on } \Gamma. \end{aligned} \tag{A.3}$$

Then $\tilde{\alpha}$ is the correct gradient. This explains the smoothing in (5.3).

References

[1] M. Botz, A. Emiroglu, K. Osterminski, M. Raith, R. Wčhner, C. Grosse, Überwachung und Modellierung der Tragstruktur von Windenergieanlagen, vol. 41, Beton- und Stahlbetonbau, 2020, pp. 342–354.
[2] Thomas Planès, Eric Larose, A review of ultrasonic coda wave interferometry in concrete, Cem. Concr. Res. 53 (2013) 248–255.
[3] S. Grabke, F. Clauss, K.-U. Bletzinger, M.A. Ahrens, P. Mark, R. Wüchner, Damage detection at a reinforced concrete specimen with coda wave interferometry, Materials 14 (2021) 5013.
[4] S. Grabke, K.-U. Bletzinger, R. Wüchner, Development of a finite element-based damage localization technique for concrete by applying coda wave interferometry, Eng. Struct. 269 (2022) 114585.
[5] Peter Cawley, Robert Darius Adams, The location of defects in structures from measurements of natural frequencies, J. Strain Anal. Eng. Des. 14 (2) (1979) 49–57.
[6] Pierre Ladevèze, Djamel Nedjar, Marie Reynier, Updating of finite element models using vibration tests, AIAA J. 32 (7) (1994) 1485–1491.
[7] N.M.M. Maia, J.M.M. Silva, RPC Sampaio, Localization of damage using curvature of the frequency-response-functions, in: Proceedings of the 15th International Modal Analysis Conference, vol. 3089, 1997, p. 942.
[8] Hansang Kim, Hani Melhem, Damage detection of structures by wavelet analysis, Eng. Struct. 26 (3) (2004) 347–362.
[9] Magdalena Rucka, Krzysztof Wilde, Application of continuous wavelet transform in vibration based damage detection method for beams and plates, J. Sound Vib. 297 (3–5) (2006) 536–550.
[10] Guillaume Puel, Denis Aubry, Using mesh adaption for the identification of a spatial field of material properties, Internat. J. Numer. Methods Engrg. 88 (3) (2011) 205–227.
[11] S.C. Mohan, Dipak Kumar Maiti, Damodar Maity, Structural damage assessment using FRF employing particle swarm optimization, Appl. Math. Comput. 219 (20) (2013) 10387–10400.
[12] Ludovic Chamoin, Pierre Ladevèze, Julien Waeytens, Goal-oriented updating of mechanical models using the adjoint framework, Comput. Mech. 54 (6) (2014) 1415–1430.
[13] Akbar Mirzaee, Reza Abbasnia, Mohsenali Shayanfar, A comparative study on sensitivity-based damage detection methods in bridges, Shock Vib. 2015 (2015).
[14] Gregory Bunting, Scott T Miller, Timothy F Walsh, Clark R Dohrmann, Wilkins Aquino, Novel strategies for modal-based structural material identification, Mech. Syst. Signal Process. 149 (2021) 107295.
[15] Nizar Faisal Alkayem, Maosen Cao, Yufeng Zhang, Mahmoud Bayat, Zhongqing Su, Structural damage detection using finite element model updating with evolutionary algorithms: a survey, Neural Comput. Appl. 30 (2018) 389–411.
[16] Daniele Di Lorenzo, Victor Champaney, Claudia Germoso, Elias Cueto, Francisco Chinesta, Data completion, model correction and enrichment based on sparse identification and data assimilation, Appl. Sci. 12 (15) (2022) 7458.
[17] Thomas Borrvall, Joakim Petersson, Topology optimization of fluids in Stokes flow, Internat. J. Numer. Methods Fluids 41 (1) (2003) 77–107.
[18] Boyan Stefanov Lazarov, Ole Sigmund, Filters in topology optimization based on Helmholtz-type differential equations, Internat. J. Numer. Methods Engrg. 86 (6) (2011) 765–781.
[19] Maher Salloum, David B. Robinson, Optimization of flow in additively manufactured porous columns with graded permeability, AIChE J. 68 (9) (2022) e17756.
[20] D. Thomas Seidl, Assad A. Oberai, Paul E. Barbone, The Coupled Adjoint-State Equation in forward and inverse linear elasticity: Incompressible plane stress, Comput. Methods Appl. Mech. Engrg. 357 (2019) 112588.
[21] Fredi Tröltzsch, Optimal Control of Partial Differential Equations: Theory, Methods, and Applications, vol. 112, American Mathematical Soc., 2010.
[22] Harbir Antil, Drew P Kouri, Martin-D Lacasse, Denis Ridzal, Frontiers in PDE-constrained optimization, vol. 163, Springer, 2018.
[23] Rainald Löhner, Harbir Antil, Determination of volumetric material data from boundary measurements: Revisiting Calderon's problem, Internat. J. Numer. Methods Heat Fluid Flow (2020).
[24] Olek C. Zienkiewicz, Robert Leroy Taylor, Jian Z. Zhu, The Finite Element Method: Its Basis and Fundamentals, Elsevier, 2005.
[25] Juan C. Simo, Thomas J.R. Hughes, Computational Inelasticity, vol. 7, Springer Science & Business Media, 2006.
[26] Laura Mainini, Karen Willcox, Surrogate modeling approach to support real-time structural assessment and decision making, AIAA J. 53 (6) (2015) 1612–1626.
[27] Francisco Chinesta, Elias Cueto, Emmanuelle Abisset-Chavanne, Jean Louis Duval, Fouad El Khaldi, Virtual, digital and hybrid twins: a new paradigm in data-based engineering and engineered data, Arch. Comput. Methods Eng. 27 (2020) 105–134.
[28] Rainald Löhner, Applied Computational Fluid Dynamics Techniques: An Introduction Based on Finite Element Methods, John Wiley & Sons, 2008.
[29] Rainald Löhner, FEELAST user's manual, Fairfax, Virginia, 2023.
[30] Guido Dhondt, Calculix user's manual version 2.20, Munich, Germany, 2022.
[31] Artūras Kilikevičius, Darius Bačinskas, Jaroslaw Selech, Jonas Matijošius, Kristina Kilikevičienė, Darius Vainorius, Dariusz Ulbrich, Dawid Romek, The influence of different loads on the footbridge dynamic parameters, Symmetry 12 (4) (2020) 657.
[32] Harbir Antil, Sergey Dolgov, Akwum Onwunta, TTRISK: Tensor train decomposition algorithm for risk averse optimization, Numer. Linear Algebra Appl. (2022) e2481, URL https://onlinelibrary.wiley.com/doi/abs/10.1002/nla.2481.
[33] Harbir Antil, Sergey Dolgov, Akwum Onwunta, State-constrained optimization problems under uncertainty: A tensor train approach, 2023, arXiv preprint arXiv:2301.08684.